



## **A dusty protocluster surrounding the binary galaxy HerBS-70 at $z = 2.3$**

Downloaded from: <https://research.chalmers.se>, 2025-12-05 04:39 UTC

Citation for the original published paper (version of record):

Bakx, T., Berta, S., Dannerbauer, H. et al (2024). A dusty protocluster surrounding the binary galaxy HerBS-70 at  $z = 2.3$ . Monthly Notices of the Royal Astronomical Society, 530(4): 4578-4596.  
<http://dx.doi.org/10.1093/mnras/stae1155>

N.B. When citing this work, cite the original published paper.

# A dusty protocluster surrounding the binary galaxy HerBS-70 at $z = 2.3$

Tom J. L. C. Bakx<sup>1,2,3</sup>★, S. Berta<sup>4</sup>, H. Dannerbauer<sup>5,6</sup>, P. Cox<sup>7</sup>, K. M. Butler<sup>4</sup>, M. Hagimoto<sup>8</sup>,  
D. H. Hughes<sup>8</sup>, D. A. Riechers<sup>9</sup>, P. P. van der Werf<sup>10</sup>, C. Yang<sup>11</sup>, A. J. Baker<sup>11,12</sup>, A. Beelen<sup>13</sup>,  
G. J. Bendo<sup>14</sup>, E. Borsato<sup>15</sup>, V. Buat<sup>16</sup>, A. R. Cooray<sup>17</sup>, L. Dunne<sup>18</sup>, S. Dye<sup>19</sup>, S. Eales<sup>18</sup>,  
R. Gavazzi<sup>7,20</sup>, A. I. Harris<sup>21</sup>, D. Ismail<sup>16</sup>, R. J. Ivison<sup>22</sup>, B. Jones<sup>23</sup>, M. Krips<sup>4</sup>, M. D. Lehnert<sup>24</sup>,  
L. Marchetti<sup>25,26</sup>, H. Messias<sup>27,28</sup>, M. Negrello<sup>18</sup>, R. Neri<sup>4</sup>, A. Omont<sup>7</sup>, I. Perez-Fournon<sup>5,29</sup>,  
A. Nanni<sup>30,31</sup>, N. Chartab<sup>10,32,33</sup>, S. Serjeant<sup>34</sup>, F. Stanley<sup>4</sup>, Y. Tamura<sup>2</sup>, S. A. Urquhart<sup>34</sup>,  
C. Vlahakis<sup>35</sup>, A. Weiß<sup>36</sup> and A. J. Young<sup>11</sup>

*Affiliations are listed at the end of the paper*

Accepted 2024 April 29. Received 2024 April 26; in original form 2022 December 23

## ABSTRACT

We report on deep SCUBA-2 observations at 850  $\mu\text{m}$  and Northern Extended Millimetre Array (NOEMA) spectroscopic measurements at 2 mm of the environment surrounding the luminous, massive ( $M_* \approx 2 \times 10^{11} M_\odot$ ) *Herschel*-selected source HerBS-70. This source was revealed by previous NOEMA observations to be a binary system of dusty star-forming galaxies at  $z = 2.3$ , with the east component (HerBS-70E) hosting an active galactic nucleus. The SCUBA-2 observations detected, in addition to the binary system, 21 sources at  $>3.5\sigma$  over an area of  $\sim 25$  square comoving Mpc with a sensitivity of  $1\sigma_{850} = 0.75$  mJy. The surface density of continuum sources around HerBS-70 is three times higher than for field galaxies. The NOEMA spectroscopic measurements confirm the protocluster membership of three of the nine brightest sources through their CO(4–3) line emission, yielding a volume density 36 times higher than for field galaxies. All five confirmed sub-mm galaxies in the HerBS-70 system have relatively short gas depletion times (80–500 Myr), indicating the onset of quenching for this protocluster core due to the depletion of gas. The dark matter halo mass of the HerBS-70 system is estimated around  $5 \times 10^{13} M_\odot$ , with a projected current-day mass of  $10^{15} M_\odot$ , similar to the local Virgo and Coma clusters. These observations support the claim that DSFGs, in particular the ones with observed multiplicity, can trace cosmic overdensities.

**Key words:** galaxies: clusters: general – galaxies: evolution – galaxies: high-redshift – submillimetre: galaxies.

## 1 INTRODUCTION

The evolution of the cosmic star formation rate (SFR) density (Madau & Dickinson 2014) paints a dynamic picture of galaxy evolution, with rapid stellar build-up at redshifts above 2, followed by a stark drop in SFRs of galaxies towards the present day. The origins of this down-turn are likely due to a mixture of feedback processes, broadly categorized as caused by *environmental* (strangulation, harassment, and ram-pressure stripping) and *internal* [star formation and active galactic nuclei (AGNs)] quenching effects (e.g. Peng, Maiolino & Cochrane 2015; Man & Belli 2018; Walter et al. 2020).

Cosmic overdensities form pockets where the Universe is matter-dominated, and can trace galaxy evolution in more extreme environments, where the processes that characterize star formation (i.e. fueling and feedback) happen on faster time-scales and at earlier epochs (Chiang, Overzier & Gebhardt 2013; Muldrew, Hatch & Cooke 2015; Contini et al. 2016; Overzier 2016). Notably, models predict that the majority of high-redshift star formation occurs in

overdense environments, where the compact regions drive gas away by environmental quenching through processes of gas stripping and the cessation of infalling gas that feeds star formation. Meanwhile, the rapid evolution of galaxies can trigger AGNs that disrupt gas flow and star formation from within (Vayner et al. 2021).

Hydrodynamical and parametric models of galaxy clusters predict that the intracluster medium (ICM) becomes too warm to readily collapse on to galaxies at redshifts 3–5, needing to form *cold streams* that fuel star formation until  $z \sim 2$ –3 (e.g. Dekel & Birnboim 2006). Cold flows could still persist further into the local Universe; however, their extent might be more limited (Dressler 1980; Webb et al. 2015, 2017; Trudeau et al. 2019; Finner et al. 2020; Hlavacek-Larrondo et al. 2020). This generic picture (Shimakawa et al. 2018) then predicts rapid quenching through a lack of fueling of the central galaxies, resulting in passive galaxy clusters at redshift 0 such as the  $\sim 10^{15} M_\odot$  Virgo cluster (Fouqué et al. 2001). In particular, this sudden lack of inflowing gas in dense environments at  $z \sim 2.5$  allows for a unique test of galaxy quenching (Smail 2024).

Studies into the properties of these protocluster galaxies, however, find varying properties from protocluster to protocluster. They have measured metallicities deficient (Valentino et al. 2015) or enhanced

★ E-mail: [tom.bakx@chalmers.se](mailto:tom.bakx@chalmers.se)

(Shimakawa et al. 2015; Biffi et al. 2018) relative to field galaxies; they have SFRs boosted (Shimakawa et al. 2018) or suppressed (Tran et al. 2015) relative to field galaxies; they are more gas-rich than field galaxies (Noble et al. 2017; Tadaki et al. 2019), or show similar gas-richness (Castignani et al. 2020; Lee et al. 2021), or they show evidence of the re-distribution of metals across the galaxies through their circum-galactic medium (CGM; Wang et al. 2021).

The galaxy populations within protoclusters appear diverse, and we are currently limited in our understanding through a sheer lack of identified high- $z$  protocluster environments. This diversity, however, could also be a selection bias, since protoclusters are found across the entire electromagnetic spectrum, from UV (Steidel et al. 1998; Venemans et al. 2007; Toshikawa et al. 2012), optical (Hatch et al. 2011; Spitler et al. 2012) to radio (Galametz et al. 2013), each of which are likely sensitive to a specific galaxy population and therefore to a specific phase of cluster evolution.<sup>1</sup>

To extend these studies out to higher redshifts, various rare populations of galaxies or quasars have been proposed to trace overdense regions, with mixed results. For example, quasars have been shown to trace protoclusters by Kim et al. (2009), Utsumi et al. (2010), Morselli et al. (2014), Kikuta et al. (2017), Ota et al. (2018), Kikuta et al. (2019), and García-Vergara et al. (2022); however, the studies by Bañados et al. (2013), Goto et al. (2017), and Mazzucchelli et al. (2017) failed to reveal any overdense environments, suggesting that this method is not necessarily robust (e.g. Champagne et al. 2018).

Dusty star-forming galaxies (DSFGs; Blain et al. 2002; Casey, Narayanan & Cooray 2014; Hodge & da Cunha 2020) are known to trace some of the most active star-forming regions in the Universe, with very short gas depletion time-scales (Swinbank et al. 2014; Aravena et al. 2016a; Cañameras et al. 2018). Observational studies have shown a strong connection between these galaxies and their wider CGM (Banerji et al. 2011; Dannerbauer et al. 2014; Emonts et al. 2016, 2018; Spilker et al. 2020a, b; Berta et al. 2021; Butler et al. 2021; Riechers et al. 2021) rapidly enriching their environments while also showcasing examples of gas feeding at  $z \sim 2-3$ . FIR cameras have successfully identified such protocluster systems, requiring multihour observations to reveal a handful to tens of components (Ivison et al. 2000; Stevens et al. 2003; De Breuck et al. 2004; Stevens et al. 2005; Chapman et al. 2009; Tamura et al. 2009; Aravena et al. 2010; Stevens et al. 2010; Capak et al. 2011; Casey et al. 2013; Dannerbauer et al. 2014; Miller et al. 2018; Zeballos et al. 2018; Gómez-Guijarro et al. 2019; Lacaille et al. 2019; Smith et al. 2019b; Guaita et al. 2022; Zhang et al. 2022). The small number of sources revealed by continuum cameras limit the statistical power of sub-mm observations (e.g. Lewis et al. 2018); however, it is important to characterize these sources, as they dominate the star formation in these environments (e.g. Casey et al. 2013; Dannerbauer et al. 2014; Busmann et al. 2015; Miller et al. 2018; Oteo et al. 2018; Long et al. 2020; Stach et al. 2021). Stacking experiments by Kubo et al. (2019) and Alberts et al. (2021) further show an excess of mid-infrared (MIR) and FIR emission from protoclusters in *Wide-field Infrared Survey Explorer* (WISE) and *Planck* data. Environmental studies of DSFGs also help characterize the evolution of the massive end of star formation, as DSFGs are the likely progenitors of massive

ellipticals, which could help identify potential environmental effects in order to explain recent observations of massive quenched galaxies being found at  $z \sim 4$  (Straatman et al. 2014; Glazebrook et al. 2017; Simpson et al. 2017; Schreiber et al. 2018; Looser et al. 2023). Meanwhile, simulations suggest that source multiplicity might be a better indicator than the more time-variable measure of SFR (Remus, Dolag & Dannerbauer 2022). In order to efficiently identify overdensities, tracing out the environments around distant DSFGs with neighbouring sources, we would address both strong selection criteria for overdense environments.

Follow-up observations of luminous high-redshift galaxies detected in large surveys such as *Herschel*, in particular using submillimetre facilities, have enabled to identify candidate protoclusters by resolving the sources in multiple galaxies at similar redshift. A recent example is the z-GAL survey that measured, using the NOEMA Extended Millimetre Array (NOEMA), precise spectroscopic redshifts of 135 dusty, bright *Herschel*-selected galaxies (Neri et al. 2020; Cox et al. 2023). In some cases, the fields displayed multiplicity and revealed candidate protoclusters. One example is the *Herschel* galaxy H-ATLAS J130140.2 + 292918 (HerBS-70), which was revealed by the NOEMA observations to be a binary system of DSFGs at  $z = 2.3$ , where the two components are separated by  $16.5''$  and the east component (HerBS-70E) hosts an AGN (Neri et al. 2020; Stanley et al. 2023).

In this work, we report on deep continuum observations at  $850 \mu\text{m}$  of the environment around HerBS-70 using SCUBA-2 on the James Clerk Maxwell Telescope (JCMT) and targeted NOEMA spectroscopic measurements of the most likely protocluster candidates in the field. In Section 2, we describe the properties of HerBS-70, and why it is a good candidate lighthouse for a cosmic overdensity. We then report on the continuum map observations using the SCUBA-2 instrument on the JCMT and spectroscopic observations using NOEMA at 2 mm, including the reduction steps, flux extraction, completion and flux boosting estimates in Section 3. Section 4 characterizes the overdensity in HerBS-70 using the spectroscopic and continuum observations. We continue our discussion on the *Herschel* photometry to produce photometric redshifts, and evaluates the continuum overdensity estimates based on source counts and spatial source distribution. Subsequently, this section places the wider environment around HerBS-70 in its cosmological context, and looks forward to expanded studies of the environments surrounding DSFGs in general. We provide our conclusions in Section 5. Throughout this paper, we assume a flat Lambda cold dark matter ( $\Lambda\text{CDM}$ ) cosmology with the best-fitting parameters derived from the *Planck* results (Planck Collaboration VI 2020), which are  $\Omega_m = 0.315$ ,  $\Omega_\Lambda = 0.685$ , and  $h = 0.674$ .

## 2 HERBS-70: A RAPIDLY QUENCHING, AGN-HOSTING SOURCE WITH A NEARBY COMPANION

As part of a redshift campaign of bright, dusty galaxies identified by *Herschel*-ATLAS (Eales et al. 2010; Bakx et al. 2018, 2020b), NOEMA observations of HerBS-70 revealed a non-lensed binary system at  $z_{\text{spec}} = 2.3$  (Neri et al. 2020; Cox et al. 2023). Table 1 summarizes the sub-mm properties of the HerBS-70 system. The two galaxies of the HerBS-70 system, HerBS-70W and HerBS-70E, are separated by a projected distance of  $16.5''$  ( $140 \text{ kpc}$  at  $z = 2.3$ ), and the spectroscopic redshift difference between the galaxies is relatively small, corresponding to a velocity shift of  $350 \text{ km s}^{-1}$  ( $z_{\text{spec}} = 2.3077$  and  $2.3155$  for HerBS-70E and -70W, respectively; Neri et al. 2020). The source HerBS-70E displays

<sup>1</sup> An important exception to this are protoclusters selected by the Sunyaev–Zeldovich effect, which can accurately trace the total mass of dark matter haloes – important for a cosmic census. However, this method becomes increasingly difficult to detect  $z > 1$  protoclusters (e.g. Di Mascolo et al. 2021; Meinke et al. 2021).

**Table 1.** Sub-mm derived properties of HerBS-70E & W.

	HerBS-70E	HerBS-70W	
$L_{\text{IR}} (10^{11} L_{\odot})$	$180.0 \pm 6.0$	$42.8 \pm 5.0$	Berta et al. (2023)
$\text{SFR} (M_{\odot} \text{ yr}^{-1})$	$2000 \pm 100$	$470 \pm 80$	Berta et al. (2023)
$M_{\text{dust}} (10^{10} M_{\odot})$	$0.42 \pm 0.04$	$0.10 \pm 0.04$	Neri et al. (2020)
$M_{\text{gas}} (10^{11} M_{\odot})$	$3.3 \pm 0.9$	$3.1 \pm 0.5$	Berta et al. (2023)
	$2.7 \pm 0.6$	$1.5 \pm 0.3$	Stanley et al. (2023)
$t_{\text{depl}} (10^9 \text{ yr})$	$0.17 \pm 0.06$	$0.66 \pm 0.11$	Berta et al. (2023)

strong double-peaked emission lines of CO (3–2) and (4–3) with widths of  $\sim 770 \text{ km s}^{-1}$ . In contrast, HerBS-70W has significantly narrower ( $\sim 140 \text{ km s}^{-1}$ ) single-peaked emission lines. Subsequent observations using the VLA measured the CO(1–0) emission line of the HerBS-70 binary system and revealed a bright radio continuum at 30 GHz in HerBS-70E indicating the presence of a radio luminous AGN in this source (Stanley et al. 2023). Based on these results, the following properties were derived for HerBS-70E and W. The 8–1000  $\mu\text{m}$  infrared luminosities are  $1.8 \times 10^{13}$  and  $4 \times 10^{12} L_{\odot}$  for HerBS-70 E and W, respectively, yielding SFRs of 2000 and  $470 M_{\odot} \text{ yr}^{-1}$ , assuming a Chabrier (2003) initial mass function (Berta et al. 2023), and dust masses of 4 and  $1 \times 10^9 M_{\odot}$  (Draine & Li 2007; Neri et al. 2020). The molecular gas masses of HerBS-70E and W are  $2.7 \times 10^{11}$  and  $1.5 \times 10^{11} M_{\odot}$ , with estimated depletion time-scales of 170 and 660 Myr, respectively, although these values vary strongly between different gas-mass and star formation estimates (Berta et al. 2023; Stanley et al. 2023).

HerBS-70E poses an interesting case of feedback through multiple mechanisms. First, the detection of a buried AGN in HerBS-70E suggests ongoing quenching through negative feedback (Stanley et al. 2023). Secondly, star formation feedback is likely present, given the excessive  $\sim 1500\text{--}3000 M_{\odot} \text{ yr}^{-1}$  SFR of HerBS-70E (Rowan-Robinson et al. 2016). Finally, the depletion time-scale (i.e. the star-forming gas mass divided by the SFR) is on the order of 170 Myr (Swinbank et al. 2014; Bakx et al. 2020c; Berta et al. 2023; Stanley et al. 2023), which places a strong limit on the quenching time-scale in the case of no inflowing gas.

In order to better understand HerBS-70E and its potential for being a central source in an overdense region, we reproduced the UV-to-radio spectral energy distribution (SED) with a composite model that includes the emission of stars, of dust heated by stellar light and by an AGN dusty torus (see Fig. 1). We adopted the SED3FIT code (Berta et al. 2013), which combines Bruzual & Charlot (2003) stellar models, dust emission powered by star formation (see also da Cunha, Charlot & Elbaz 2008), and an AGN torus component (Fritz, Franceschini & Hatziminaoglou 2006; Feltre et al. 2012, 2013), fitted simultaneously to the observed SED.

The radio continuum is not directly fitted by the code, it is instead computed from the model IR luminosity adopting the radio–FIR correlation at the redshift of HerBS-70E (Delhaize et al. 2017, see also Magnelli et al. 2015). The expected radio emission due to star formation (grey solid line of Fig. 1) is much weaker than the observed radio continuum fluxes. This excess confirms the presence of an AGN in the central regions of HerBS-70E (see also Stanley et al. 2023). The *WISE* data reveal a MIR excess in the broad-band SED, that is fitted with an AGN torus (see green long-dashed line in Fig. 1).

An additional radio power law (dotted grey line in Fig. 1) is added a posteriori to reproduce the radio emission of the HerBS-70E central AGN. At the lowest frequencies, the LOFAR data suggest a change of slope of the radio emission. This change of slope is mainly due to synchrotron self-absorption (SSA), but note that the low-frequency

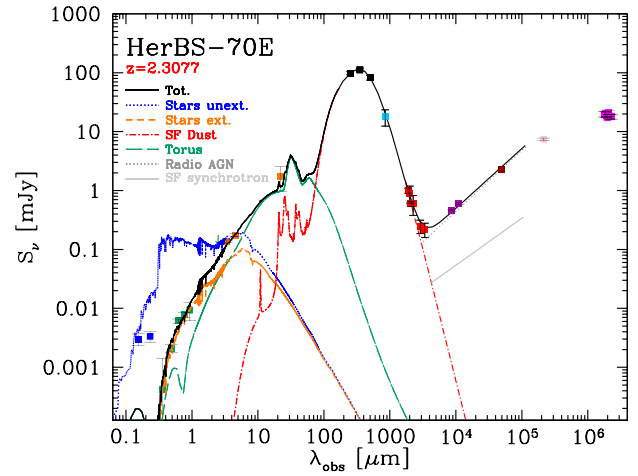


**Figure 1.** The UV-to-radio SED fit of HerBS-70E shows different emission components across the various wavelength ranges. The sub-mm emission is dominated by the dust obscuring star formation, while the AGN component is dominant at near-infrared and radio wavelengths. The fit is performed using the SED3FIT code (Berta et al. 2013), and uses data from GALEX (UV; blue squares), SDSS (optical; green squares), UKIDSS (near-infrared; green squares), WISE (MIR; orange squares), Herschel H-ATLAS (FIR; black squares), SCUBA-2 (this paper light-blue squares), NOEMA (mm; Neri et al. 2020; dark-red squares), VLA (radio; purple squares), Faint Images of the Radio Sky at Twenty centimeters (FIRST) and Low Frequency ARray (LOFAR; m-wavelength; Stanley et al. 2023; brown, salmon, and pink squares). The expected radio emission based on the FIR-radio correlation of Delhaize et al. (2017) at the redshift of HerBS-70E is shown as a grey line beyond  $10^4 \mu\text{m}$ , and is well below the observed radio flux densities. The excess emission is due to AGN contribution (dotted grey line). Similarly at the MIR, excess emission in *WISE* is fit by a power-law-like SED indicative of a dusty torus at the centre of HerBS-70.

spectral index is shallower than that of pure SSA, thus indicating that also other physical processes influence it.

The total  $L(\text{IR}, 8\text{--}1000 \mu\text{m})$  of the source is between  $1.6$  and  $2.9 \times 10^{13} L_{\odot}$ , with the contribution of star formation amounting between  $1.4$  and  $2.6 \times 10^{13} L_{\odot}$ . The latter corresponds to an SFR in the range of  $\sim 1500\text{--}2800 M_{\odot} \text{ yr}^{-1}$ , adopting the Kennicutt (1998) conversion after correcting it to the Chabrier (2003) IMF.

The inclusion of the AGN component is important to estimate the stellar mass, because the near-infrared emission of HerBS-70E turns out to be dominated by the dusty torus ( $\sim 60$  per cent between  $1.0$  and  $2.5 \mu\text{m}$  and up to  $\sim 90$  per cent between  $2.5$  and  $5.0 \mu\text{m}$ ). The resulting best-fitting stellar mass is  $2.0^{+0.4}_{-0.5} \times 10^{11} M_{\odot}$ . This suggests a low specific SFR (SFR per unit stellar mass or a stellar-mass doubling time-scale) of  $70\text{--}130 \text{ Myr}^{-1}$ . Combined with the available molecular gas from CO emission, this implies a gas fraction on the order of  $\sim 60$  per cent (see also Neri et al. 2020; Ismail et al. 2023; Stanley et al. 2023), in line with soon-to-be quenched galaxies (Gobat et al. 2018, 2020) at both low and high redshifts.

Although no conclusive evidence yet exists, there are several indications that point to the presence of a cosmic overdensity (Overzier 2016): (i) HerBS-70E is forming stars at a high rate ( $\sim 1500\text{--}3800 M_{\odot} \text{ yr}^{-1}$ ), while having an additional galaxy in its vicinity that could indicate an overdensity of objects within its environment (HerBS-70W). (ii) Meanwhile, HerBS-70E has already built up a significant stellar mass at less than three billion years after the Big Bang, which would mean an average SFR of at least  $\sim 70 M_{\odot} \text{ yr}^{-1}$ . These SFRs in the early Universe are primarily seen in overdense regions in the early Universe (Chiang et al. 2017). (iii)



The stellar assembly further required a large amount of gas and/or efficient feeding of galaxy to reach  $2 \times 10^{11} M_{\odot}$ , and HerBS-70E is currently rapidly processing all remaining gas within its system ( $t_{\text{dep}} = 170$  Myr). Although the presence of an AGN can drive quenching – and is predicted to amply exist in  $z = 2$  protoclusters (Shimakawa et al. 2018) – it is also possible that galaxies in its environment are removing gas flows needed for future star formation. Since many of these indications are found together in the HerBS-70 system, a characterization of its environment can teach us both about the evolution of massive galaxies and about large-scale structures in the Universe.

### 3 OBSERVATIONS AND RESULTS

In order to find evidence that the binary system HerBS-70 is part of a protocluster, we first carried out deep 850  $\mu\text{m}$  continuum observations using the SCUBA-2 sub-millimetre camera to search for DSFGs in the Mpc-scale environment around HerBS-70. These observations were followed-up by targeted spectroscopic measurements with NOEMA of selected sources identified in the 850  $\mu\text{m}$  continuum map in order to derive their spectroscopic redshifts and verify that the values are around  $z \sim 2.3$ , comparable to HerBS-70. In this Section, we discuss the SCUBA-2 and NOEMA observations and results, including data reduction, flux extraction steps, as well as produce estimates of the completeness and flux boosting.

#### 3.1 Continuum map with SCUBA-2

The mapping speed of sub-mm spectroscopic instruments is relatively low, which favours a two-step process in identifying overdense regions. First, a fast continuum mapping observation characterizes dusty galaxies, and these sources can then be observed through targeted spectroscopic follow-up. Here, we use SCUBA-2 on JCMT to look for dusty galaxies in the vicinity of the HerBS-70 system.

##### 3.1.1 SCUBA-2 850 $\mu\text{m}$ observations

HerBS-70 was observed using the SCUBA-2 bolometer instrument mounted on the JCMT. The instrument is able to observe both 450 and 850  $\mu\text{m}$  emission simultaneously through a dichroic mirror (Holland et al. 2013). Through a DAISY pattern scanning observations, HerBS-70 was observed following a continuous petal-like track, providing a central 3 arcmin region of uniform exposure time, and keeping one part of the array on-source at all times (Chapin et al. 2013). The observations were conducted under project code M20BP049 (PI: T. Bakx) in excellent weather conditions ( $\tau_{225} \approx 0.04\text{--}0.06$ ) on the 29th of January, the 1st and 3rd of February 2021 for a total of 4.9 h of on-source time.

##### 3.1.2 Data reduction

We followed the *zero masking* data reduction prescription described in Holland et al. (2017), which performs the standard deep observation pipeline using the STARLINK’s SMURF and KAPPA packages. This observation pipeline is supplemented with the addition of masking into the central bright source that was previously detected with *Herschel* and NOEMA. The data is reduced iteratively using the MAP-MAKER algorithm, which removes noise in order to produce a final astronomical estimate in the image plane. This assumed astronomical signal is then removed from the time-series data, and the noise estimations are done again until a threshold noise level is reached.

The resulting astronomical map is then *matched filtered* to the point spread function (PSF) of the JCMT, assumed to be 13 arcsec. The assumed flux-conversion-factor is taken to be  $537 \text{ Jy pW}^{-1} \text{ beam}^{-1}$  (Smith et al. 2019a; Mairs et al. 2021). The signal-to-noise ratio (SNR) map is produced using the KAPPA recipe MAKESNR. At the centre of the map, the noise level is  $0.75 \text{ mJy beam}^{-1}$ , which approaches the background-confusion limit due to the far-infrared (FIR) background caused by unresolved sub-mm emitters within the beam of the JCMT.

Fluxes are extracted using the matched-filtered signal-to-noise map using the peak emission value. Sources are differentiated by emission peaks separated by more than one beam (13 arcsec), and each source should have at least  $3.5\sigma$ . None of the sources are extended beyond the JCMT beam. Noise estimates are made directly from the noise map, which is also produced by the MAKEMAP algorithm.

Fig. 2 shows the resulting map of around 14 by 14 arcmin, with all sources above  $3.5\sigma$  marked as stars, with sources  $>5\sigma$  displayed with larger stars. Thin dashed lines indicate the regions where the background noise is below 2, 5, and 10 mJy. In total, 21 SCUBA-2 sources are identified at  $>3.5\sigma$  in addition to HerBS-70 (the E and W components are not resolved in the SCUBA-2 image), and are labelled according to decreasing SNR ratio (Table 2). An inset of the NOEMA 2-mm continuum map is shown in the top-right corner (from Neri et al. 2020), where HerBS-70E and 70W are seen as resolved sources. Green squares show the sources with nearby *Herschel* galaxies identified through the HELP catalogue<sup>2</sup> (Shirley et al. 2021). The *light-blue* contours show the regions where the field is denser than thrice the expected number of background sources (see Section 4.2.3).

Fig. 3 shows the distribution of SNR values of each pixel in the map. Broadly, the bulk of the pixels follow the behaviour expected from white noise, i.e. a Gaussian fit with  $\sigma = 1$  fits the bulk of the data well. Several peaks at the low and high end of the SNR distribution indicate the existence of sources. The negative pixels are caused by the PSF of the JCMT beam, which has negative rings around the peak of  $\sim 20$  percent of the peak flux. Excess noise pixels around  $\sim -5\sigma$  are thus expected given the peak SNR of around  $20\sigma$ .

##### 3.1.3 Completeness and flux boosting

In order to maximize the scientific gain of the SCUBA-2 image, we assessed the contamination (i.e. false-positives) and completeness (i.e. false-negatives) of our SCUBA-2 observations, and corrected for the Eddington bias in the flux boosting. The Eddington bias accounts for the observed upward boost of fluxes, since there are more faint galaxies that scatter upwards than there are rarer bright galaxies that scatter towards fainter fluxes. Here, we broadly follow the procedure documented in Eales et al. (2000), Cowie, Barger & Kneib (2002), Scott et al. (2002), Borys et al. (2003), Coppin et al. (2006), Lewis et al. (2018), and in line with recent deep SCUBA-2 observations such as the SCUBA-2 Cosmological Legacy Survey (Geach et al. 2017) and the SCUBA-2 survey of COSMOS (Casey et al. 2013; Simpson et al. 2019).

We use the negative map of the SCUBA-2 image as a reference image without source emission. We first process this map by removing any spurious identifications above  $2.5\sigma$  and below  $-2.5\sigma$ , and proceed to add fake sources based on the source count distribution

<sup>2</sup><http://herschel.sussex.ac.uk>

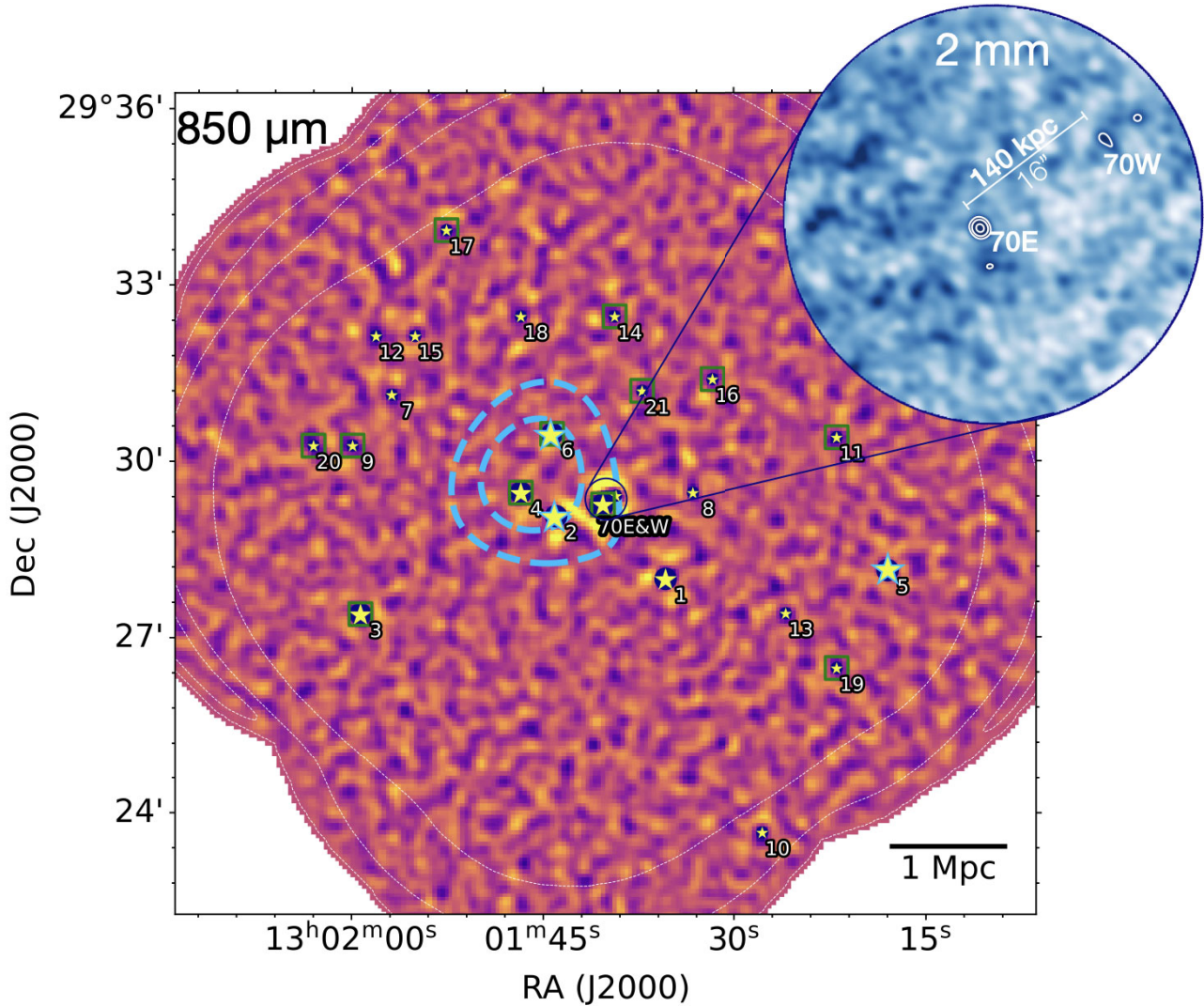


**Figure 2.** The SCUBA-2 850  $\mu\text{m}$  SNR map of a  $14 \times 14 \text{ arcmin}^2$  area centred on HerBS-70, equivalent to  $7 \times 7 \text{ Mpc}$  at  $z = 2.3$ . In total, seven sources are detected at  $>5\sigma$  (large stars), including the binary system HerBS-70 (unresolved by SCUBA-2), and fifteen sources are detected at  $>3.5\sigma$  (small stars). The spectroscopically confirmed sources from the NOEMA observations are identified by stars with blue borders, i.e. H70.2, 0.5, and 0.6. The sources H70.1, 0.3, 0.4, 0.7, 0.8, and 0.10 were found to not be close in redshift to HerBS-70. Thin dashed contours indicate the flux standard deviation at 2, 5, and 10 mJy. The blue dashed contours indicate the regional overdensity on the scales of  $\sim 1 \text{ arcmin}$  ( $\sim 0.5 \text{ Mpc}$ ) of the map, based on field number count statistics from Geach et al. (2017) which account for the inhomogeneous survey depth (see Section 4.2.3). Sources with nearby *Herschel* identifications are shown with green boxes (Section 4.2.1). Four sources at  $>5\sigma$  are located within 1 Mpc of the central source at a surface density in excess of 2.9 times that of field galaxies (see the text for details). This overdensity suggests HerBS-70 is located at the centre of a protocluster core. The inset figure shows the 150 GHz continuum emission (background and contours) centred on the position of HerBS-70E, with HerBS-70W at 140 kpc (16 arcsec) projected distance. Both sources have robust spectroscopic redshifts from detections of CO(1–0), CO(3–2), and CO(4–3) emission lines at  $z = 2.307$  and 2.315, respectively (Neri et al. 2020; Stanley et al. 2023). No additional sources are located behind the inset figure.

from Weiß et al. (2009), assuming the typical full width at half-maximum (FWHM) of the beam (13 arcsec). We execute this process 5000 times and extract our galaxies through their peak point-source flux, which we then compare it against the original *injected* flux. We then use the noise maps to translate the *injected* fluxes into SNR estimates.

Fig. 4 compares the *injected* sources within each SNR bin to the fraction of sources that were actually extracted, as shown in the blue points *completeness* graph, i.e. the false-negatives. Even down to  $3\sigma$ , we are able to extract 75 per cent of the sources. The *orange contamination* graph indicates the fraction of spurious sources that are extracted, i.e. the false-positives. The errors on both estimates are

proportional to the square root of the number of simulated sources in each SNR bin. The number of contaminants increases rapidly below  $4\sigma$ , even suggesting that up to 75 per cent of  $3\sigma$  sources are spurious. As a balance between contamination and completion, we take a  $3.5\sigma$  cut as an extraction threshold.

Fig. 5 shows the Eddington boosting depending on the SNR of a source. The Eddington boosting is calculated as the ratio between the measured and the injected flux. Galaxies detected at lower SNR are more likely to be boosted in flux due to the exponential nature of the source count distribution, with the faintest sources typically appearing  $\sim 20$  per cent brighter than their true flux. We therefore appropriately adjust for the flux boosting for the 850  $\mu\text{m}$  fluxes in

**Table 2.** Observed and derived properties of sources detected at 850  $\mu\text{m}$  in the field surrounding HerBS-70.

#	RA (hms)	DEC (dms)	SNR	$z_{\text{phot}}$	$\text{SFR}_{850}$ ( $\text{M}_{\odot} \text{yr}^{-1}$ )	$L_{\text{IR}}$ ( $10^{12} L_{\odot}$ )	$M_{\text{dust}}$ ( $10^9 \text{M}_{\odot}$ )	$S_{250 \mu\text{m}}$ (mJy)	$S_{350 \mu\text{m}}$ (mJy)	$S_{500 \mu\text{m}}$ (mJy)	$S_{850 \mu\text{m}}$ (mJy)	Bias	$\mathcal{F}$
70EW	13:01:40.3	+ 29:29:16	22.6	$1.8 \pm 0.4$	1800	10.2	5.3	$122.3 \pm 6.1$	$139.3 \pm 5.6$	$106.4 \pm 6.0$	$16.9 \pm 1.9$	1.00	0.0
70S1	13:01:35.4	+ 29:28:00	8.9	$3.4 \pm 0.6$	780	4.6	2.4	$11.9 \pm 6.1^a$	$12.6 \pm 5.6^a$	$15.7 \pm 6.0^a$	$7.5 \pm 1.2$	1.00	0.0
70S2	13:01:44.0	+ 29:29:04	6.8	$2.0 \pm 0.4$	550	3.2	1.7	$23.3 \pm 6.1^a$	$32.4 \pm 5.6^a$	$28.7 \pm 6.0^a$	$5.3 \pm 1.1$	1.01	0.0
70S3	13:02:00.3	+ 29:27:24	6.6	$1.7 \pm 0.4$	750	4.4	2.3	$54.0 \pm 6.0$	$57.5 \pm 5.5$	$40.3 \pm 6.3$	$7.2 \pm 1.5$	1.01	0.0
70S4	13:01:46.7	+ 29:29:28	6.5	$1.7 \pm 0.4$	580	3.4	1.8	$34.2 \pm 6.1$	$37.4 \pm 5.6$	$20.6 \pm 6.1$	$5.6 \pm 1.2$	1.01	0.0
70S5	13:01:18.0	+ 29:28:08	5.1	$2.6 \pm 0.5$	670	3.9	2.0	$16.3 \pm 6.1^a$	$19.5 \pm 5.6^a$	$12.8 \pm 6.0^a$	$6.5 \pm 1.8$	1.01	0.0
70S6	13:01:44.3	+ 29:30:28	5.0	$2.0 \pm 0.4$	430	2.5	1.3	$17.9 \pm 6.0$	$19.8 \pm 5.3$	$6.5 \pm 6.3$	$4.2 \pm 1.2$	1.01	0.0
70S7	13:01:56.9	+ 29:31:08	4.7	$3.5 \pm 0.6$	540	3.1	1.6	$6.2 \pm 6.1^a$	$9.5 \pm 5.6^a$	$12.5 \pm 6.0^a$	$5.2 \pm 1.6$	1.01	0.0
70S8	13:01:33.3	+ 29:29:28	4.3	$2.8 \pm 0.5$	400	2.3	1.2	$6.1 \pm 6.1^a$	$13.2 \pm 5.6^a$	$6.1 \pm 6.0^a$	$3.9 \pm 1.2$	1.02	0.0
70S9	13:02:00.0	+ 29:30:16	4.3	$1.3 \pm 0.3$	520	3.0	1.6	$58.4 \pm 5.9$	$46.2 \pm 5.9$	$25.8 \pm 6.5$	$5.0 \pm 1.6$	1.02	0.0
70S10	13:01:27.8	+ 29:23:40	4.2	$3.6 \pm 0.6$	1100	6.6	3.4	$13.1 \pm 6.1^a$	$19.0 \pm 5.6^a$	$16.7 \pm 6.0^a$	$10.9 \pm 3.5$	1.02	0.0
70S11	13:01:22.0	+ 29:30:24	4.1	$0.7 \pm 0.2$	460	2.7	1.4	$102.5 \pm 6.0$	$57.1 \pm 5.2$	$29.5 \pm 6.2$	$4.4 \pm 1.5$	1.03	0.0
70S12	13:01:58.1	+ 29:32:08	3.9	$3.4 \pm 0.6$	480	2.8	1.5	$5.9 \pm 6.1^a$	$8.2 \pm 5.6^a$	$12.3 \pm 6.0^a$	$4.7 \pm 1.6$	1.05	0.1
70S13	13:01:25.9	+ 29:27:24	3.8	$2.6 \pm 0.5$	430	2.5	1.3	$8.4 \pm 6.1^a$	$17.6 \pm 5.6^a$	$29.3 \pm 6.0^a$	$4.2 \pm 1.5$	1.05	0.2
70S14	13:01:39.4	+ 29:32:28	3.7	$0.7 \pm 0.2$	510	3.0	1.6	$128.5 \pm 6.2$	$76.3 \pm 5.4$	$35.9 \pm 5.7$	$5.0 \pm 1.8$	1.06	0.2
70S15	13:01:55.0	+ 29:32:08	3.7	$2.4 \pm 0.4$	420	2.5	1.3	$12.0 \pm 6.1^a$	$16.7 \pm 5.6^a$	$22.0 \pm 6.0^a$	$4.1 \pm 1.5$	1.06	0.2
70S16	13:01:31.7	+ 29:31:24	3.7	$2.3 \pm 0.4$	370	2.2	1.1	$16.5 \pm 5.8$	$5.7 \pm 5.8$	$3.6 \pm 6.4$	$3.6 \pm 1.3$	1.06	0.2
70S17	13:01:52.6	+ 29:33:56	3.7	$2.1 \pm 0.4$	630	3.7	1.9	$21.2 \pm 5.8$	$18.2 \pm 5.7$	$8.8 \pm 6.0$	$6.1 \pm 2.2$	1.06	0.3
70S18	13:01:46.8	+ 29:32:28	3.7	$1.7 \pm 0.4$	400	2.3	1.2	$23.4 \pm 6.1^a$	$17.2 \pm 5.6^a$	$10.1 \pm 6.0^a$	$3.9 \pm 1.4$	1.06	0.3
70S19	13:01:22.0	+ 29:26:28	3.6	$1.5 \pm 0.3$	480	2.8	1.4	$30.3 \pm 6.0$	$20.4 \pm 5.5$	$9.9 \pm 6.0$	$4.6 \pm 1.7$	1.07	0.3
70S20	13:02:03.0	+ 29:30:16	3.5	$1.6 \pm 0.3$	410	2.4	1.2	$38.0 \pm 5.8$	$31.3 \pm 5.6$	$27.3 \pm 5.7$	$4.0 \pm 1.5$	1.08	0.4
70S21	13:01:37.3	+ 29:31:12	3.5	$1.9 \pm 0.4$	310	1.8	0.9	$13.6 \pm 5.6$	$16.5 \pm 5.7$	$3.7 \pm 5.9$	$3.0 \pm 1.1$	1.08	0.4

*Note.* Column 1: The source identification of the sources shown in Fig. 2. Columns 2 and 3: The right ascension and declination of the sources. Column 4: The SNR of the sources from the map, extracted from the peak pixel using the raw signal and noise of the sources, i.e. uncorrected for Eddington bias that is included in column 12. Column 5: Photometric redshift derived using the two-temperature modified black-body from Pearson et al. (2013). Column 6: The bolometric infrared luminosity (8–1000  $\mu\text{m}$ ), derived from the deboosted 850  $\mu\text{m}$  flux density assuming  $z = 2.3$ . We assume a single-temperature modified black-body at 30 K. Column 7: The SFR derived from the FIR luminosity-to-SFR conversion factor,  $1.73 \times 10^{-10} \text{ M}_{\odot} \text{yr}^{-1} / L_{\odot}$ , is valid for a Salpeter 1 – 100  $\text{M}_{\odot}$  IMF (Kennicutt 1998). Note that these SFR estimates are based on a single-temperature estimate, and thus the HerBS-70E&W SFR estimate deviates from the full fit provided in Bakx et al. (2018, 2020b). Column 8: The dust mass estimate assuming a single-temperature modified black-body at 30 K at  $z = 2.3$ , assuming  $\kappa_d = 10.41 \text{ cm}^2 \text{ g}^{-1}$  at 1900 GHz, and scaling according to  $\kappa_d(\nu/\nu_{\text{ref}})^{\beta}$  with  $\beta = 2$  following Draine (2003). Columns 9–11: The *Herschel* photometry derived from the HELP catalogue. Column 12: The 850  $\mu\text{m}$  fluxes and errors, corrected for flux boosting, with the errors including both the instrumental and observational biases. Column 13: The flux boosting bias. Column 14: The false-positive probability, as a probability between 0 and 1. “When unavailable, we extract the fluxes directly from the *Herschel* maps ([www.h-atlas.org](http://www.h-atlas.org)) and use the errors documented in Valiante et al. (2016).



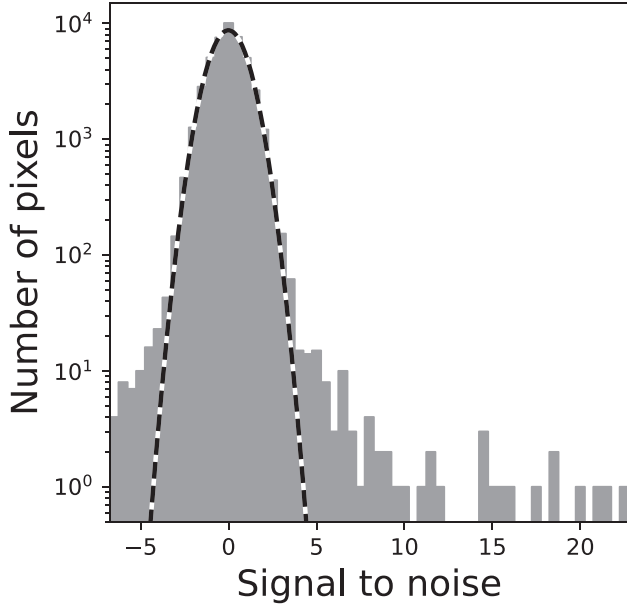


**Figure 3.** The SNR distribution of the map in Fig. 2. The majority of the data points follow the expected Gaussian ( $\sigma = 1$ ) distribution; however, the excess of bins at the positive end reflect the detection of multiple sources. At the negative tail, the excess of bins are caused by the bright nature of HerBS-70, where the negative component of the PSF of the JCMT causes deep troughs in the SNR map (Dempsey et al. 2013; Geach et al. 2017).

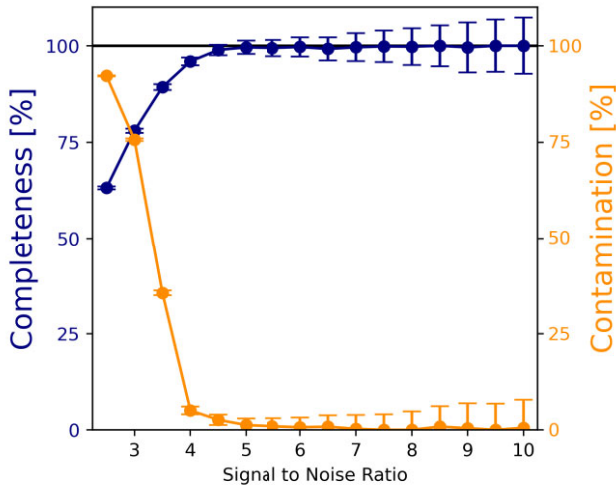


**Figure 4.** Blue markers indicate the false-negative rate of the SCUBA-2 extracted sources within each SNR bin. Sources extracted around  $3\sigma$  are around 75 per cent complete. Orange markers show the false-positive rate of the SCUBA-2 extracted sources within each SNR bin. Around 75 per cent of the sources at  $3\sigma$  are expected to be contaminants; however, the comparison of these low-fidelity sources with *Herschel* counterparts can improve the purity of this sample.

Table 2, and include the additional uncertainty to the instrumental uncertainty in quadrature.

### 3.2 Spectroscopic characterization with NOEMA

The continuum sub-mm camera observations have revealed a tentative overdensity in the central region surrounding HerBS-70

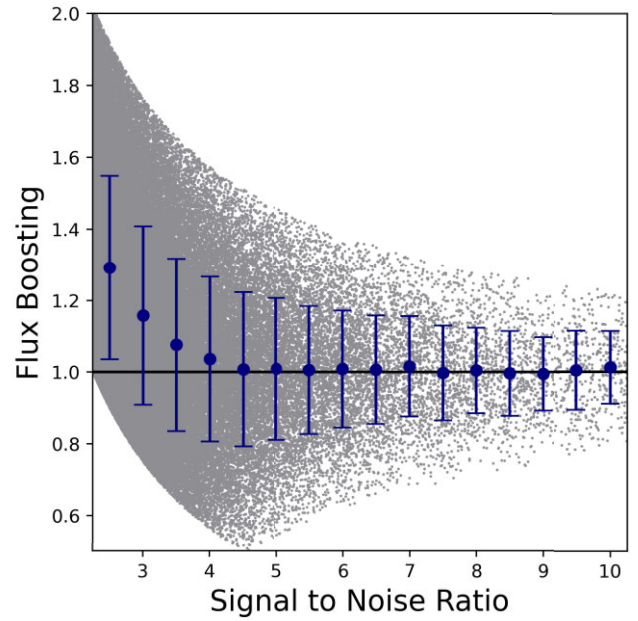


**Figure 5.** The flux boosting (i.e. the extracted/injected flux ratio) at  $850\ \mu\text{m}$  is estimated from the fake injected sources (grey dots), where the detected faint sources likely have fainter fluxes. The blue errorbars indicate the averaged flux boosting within SNR bins with a width of  $0.5\sigma$ . We adjust for the flux boosting for the  $850\ \mu\text{m}$  fluxes in Table 2, and include the additional uncertainty to the instrumental uncertainty in quadrature.

(see Section 4.2). Subsequent spectroscopic confirmation requires targeted deep observations to reveal potential spectroscopic lines. Here, we use NOEMA at 2 mm to target the CO(4–3) and [C I] emission lines simultaneously to identify companion sources at a similar redshift to the HerBS-70 system, and for those companions, measure their molecular gas masses.

#### 3.2.1 NOEMA observations of CO(4–3) and atomic carbon

During the summer of 2023, the NOEMA interferometer observed nine of the brightest protocluster member candidates in track-sharing mode (S23CI001; PI: Bakx). The source H70.9 was excluded, as it lies close to a known quasar and because of its low photometric redshift ( $z_{\text{phot}} = 1.3 \pm 0.3$ ; Table 2). The PolyFix receivers are set up to cover 132.925 to 140.625 GHz (LSB) and 148.404 to 156.104 GHz (USB), with the expected frequency for CO(4–3) is at 139.43 GHz and for [C I] is at 148.71 GHz. Fig. 6 depicts the chosen set-up to include both CO(4–3) and [C I] emission at the expected frequency of HerBS-70, and includes roughly  $\pm 2000\ \text{km s}^{-1}$  around this system, wide enough to include most of the protocluster members (Kurk et al. 2000; Koyama et al. 2013, 2021). The 2 mm band is sensitive to a brighter part of the continuum emission of protocluster members surrounding HerBS-70 and facilitate the identification of the expected position of the line emission, instead of an alternative strategy that would target CO(3–2) in the 3 mm band where the dust continuum of nearby galaxies is likely too faint to be detected.

#### 3.2.2 Data reduction and flux extraction

Phase and amplitude calibrators were chosen in close proximity to the track-shared sources in order to reduce uncertainties in astrometric and relative amplitude calibration. MWC349 and 3C273



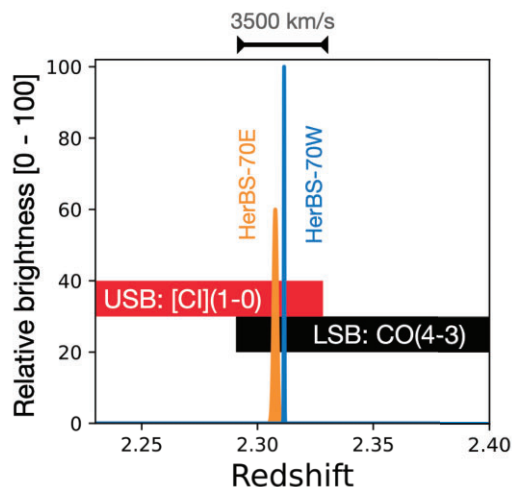


**Figure 6.** The relative emission of CO(4–3) of HerBS-70E (orange) and HerBS-70W (blue) are shown against the selected PolyFix set-ups, where the CO(4–3) and [C I] lines can be targeted in the LSB and USB, respectively. In total, the observations probe roughly  $3500 \text{ km s}^{-1}$  around HerBS-70E.

were used as absolute flux calibrators. The absolute flux calibration was estimated to be accurate to within 10 percent. The data were calibrated, averaged in polarization, imaged, and analysed in the GILDAS software package.<sup>3</sup> The  $uv$  tables were produced from calibrated visibilities in the standard way and cleaned using natural weighting and support masks defined on each of the detected sources. Continuum maps were produced for each sideband, excluding the spectral ranges that include emission lines. Continuum extraction was performed on cleaned continuum maps, after correcting for primary beam attenuation. The resulting beam size is 3.6 by 3.4 arcsec, and the continuum depth is between 60 and 90  $\mu\text{Jy beam}^{-1}$  per side-band, while the  $1\sigma$  spectral sensitivity is between 1.3 and 1.8  $\text{mJy beam}^{-1}$  in a  $35 \text{ km s}^{-1}$  bin. The spectra of each source were extracted from cleaned cubes within polygonal apertures defined by hand on the emission line channels to enhance the SNR of the spectral detection.

Table 3 shows the resulting continuum and fluxes for the nine NOEMA-observed targets. In total, four sources are detected in their dust continuum, and deep  $3\sigma$  upper limits are provided for the other five sources. For three of the sources with continuum detections, emission lines are identified in the spectroscopic NOEMA observations, which are shown in Fig. 7. H70.2 has a very wide emission line ( $\sim 960 \text{ km s}^{-1}$ ), while the H70.5 and 0.6 have much more narrow emission lines. None of the sources have accompanying [C I] line emission, suggesting the observations are not deep enough to detect the atomic carbon emission. The observed-frame wavelength of the [C I] emission of H70.6 lies outside of the observed bandwidth.

## 4 DISCUSSION

In the next sections, we present a detailed analysis of the spectroscopic observations and examine the overdensity hypothesis in light of these observations (Section 4.1). In Section 4.2, we evaluate the wider environment of HerBS-70 using the continuum observations, which was part of our motivation towards the spectroscopic observations. Section 4.3 provides a cosmological picture of the evolution of the HerBS-70 environment towards  $z = 0$ , and we conclude with

a perspective on future protocluster studies among DSFG sources (Section 4.4).

### 4.1 A gas-poor protocluster core at $z = 2.3$

As will be shown in the subsequent subsection, the continuum SCUBA-2 observations provide modest estimates of the overdensity bias of HerBS-70 ( $\delta_{\text{bias}} \approx 3$ ) through a two-dimensional perspective of the environment. The continuum observations provide only a low-significance statistic on the overdensity, exacerbated by the negative-K correction that probes infrared luminosities regardless of the source redshift (Blain 1999) which dilutes the true protocluster members with line-of-sight galaxies. Instead, the NOEMA observations are able to confirm that three additional sources are part of the HerBS-70 system, corresponding to a total additional SFR of  $1650 \text{ M}_{\odot} \text{ yr}^{-1}$  (i.e. the sum of the SFRs of H70.2, 0.5, and 0.6 from Table 2). In total, the identified system contains five dusty galaxies, and we have excluded an additional six dusty SCUBA-2 identified galaxies from the system. Finally, 10 sources remain without spectroscopic follow-up and their protocluster membership is still not known. Of the three additional sources contributing to the overdensity bias in Fig. 2, two turned out to be real protocluster members. This suggests that the continuum bias estimate ( $\delta_{\text{bias}} \approx 3$ ) is well recovered by the NOEMA observations, a surface-density bias of  $\delta_{\text{bias}} = 2$ .

The cosmic SFR density at  $z = 2.3$  is roughly  $0.063 \text{ M}_{\odot} \text{ yr}^{-1} \text{ Mpc}^{-3}$  (Madau & Dickinson 2014; Algera et al. 2023). Our observations probe a 14 by 14 arcminute region within  $\delta z = 0.04$  ( $\pm 2000 \text{ km s}^{-1}$ ) relative to the central HerBS-70 frequency. Here, the distance probed by a  $\delta z$  is equal to the difference in co-moving distances at  $z = 2.29$  and  $z = 2.33$  divided by  $(1 + z)$ . The resulting volume of  $735 \text{ Mpc}^3$  (i.e. 7 by 7 by 15 Mpc) is thus expected to contain star formation of  $46 \text{ M}_{\odot} \text{ yr}^{-1}$ . Excluding the central sources, the resulting spectroscopic overdensity is thus 36 larger than the field environment, a ten-fold increase of the overdensity estimate compared to continuum observations. If we just interpret the central region, i.e. the protocluster core identified by the SCUBA-2 observations, the star formation in this small 1 by 1 by 15 Mpc region is  $980 \text{ M}_{\odot} \text{ yr}^{-1}$  (i.e. H70.2 and 0.6). This is roughly a thousand times higher than expected from cosmic SFR density arguments.

Fig. 8 shows the molecular gas mass estimates for the NOEMA-observed sources as a function of their SFR. These are compared to known field galaxies (Scoville et al. 2016), DSFGs (Bendo et al. 2023; Hagimoto et al. 2023), known protoclusters (Zavala et al. 2019; Pérez-Martínez et al. 2023) and stacking experiments from Planck-identified regions (Alberts et al. 2021). The HerBS-70E and -70W molecular gas masses are based on the direct CO(1–0) observations reported in Stanley et al. (2023). The molecular gas masses are derived from the CO(4–3) transition, which has intrinsic uncertainty in the conversion between CO(4–3) and the ground transition CO(1–0). We use the typical equations from Solomon & Vanden Bout (2005) to convert the CO(4–3) to the line luminosity, and use the CO(4–3) to CO(1–0) conversion ratio of  $r_{4,1} = 0.46 \pm 0.07$  from Harrington et al. (2021). In this paper, we assume the CO luminosity to molecular gas conversion factor of  $\alpha_{\text{CO}} = 4.0 \text{ M}_{\odot} (\text{K km s}^{-1} \text{ pc}^2)^{-1}$  based on Dunne et al. (2021, 2022). For fair comparison, we correct all studies that use different  $\alpha_{\text{CO}}$  (typically set to  $0.8 \text{ M}_{\odot} (\text{K km s}^{-1} \text{ pc}^2)^{-1}$ ) to the value assumed in this study.

The scaling relation derived from the Scoville et al. (2016) sources, as well as the gas depletion time-scales of distant galaxies (i.e. the available molecular gas divided by the SFR) indicate that most of the sub-mm identified sources in the HerBS-70 system fall on the low end of the scaling relation with depletion times

<sup>3</sup><http://www.iram.fr/IRAMFR/GILDAS/>

**Table 3.** NOEMA fluxes of protocluster candidates.

Source	RA (hms)	Dec (dms)	$S_{\text{LSB}}$ (mJy)	$S_{\text{USB}}$ (mJy)	$z_{\text{spec}}$	$\Delta V$ (km s <sup>-1</sup> )	$\delta V_{\text{H70}}$ (km s <sup>-1</sup> )	$S_{\text{dV CO(4-3)}}$ (Jy km s <sup>-1</sup> )	$S_{\text{dV [C I]}}$ (Jy km s <sup>-1</sup> )
H70.S1	13:01:35.29	29:28:03.2	$0.43 \pm 0.08$	$0.71 \pm 0.12$					
H70.S2	13:01:44.19	29:29:03.4	$0.29 \pm 0.07$	$0.40 \pm 0.09$	2.3100	$980 \pm 160$	-205	$2.35 \pm 0.39$	<1.53
H70.S3			<0.20	<0.27					
H70.S4			<0.22	<0.29					
H70.S5	13:01:18.08	29:28:14.0	$0.39 \pm 0.09$	$0.62 \pm 0.11$	2.2895	$86 \pm 22$	-1665	$0.47 \pm 0.12$	<0.46
H70.S6	13:01:44.43	29:30:32.0	<0.24	$0.36 \pm 0.09$	2.3294	$160 \pm 36$	1947	$0.62 \pm 0.14$	-
H70.S7			<0.26	<0.27					
H70.S8			<0.20	<0.25					
H70.S10			<0.21	<0.29					

*Note.* Column 1: Source name. Columns 2 and 3: The right ascension and declination of the sources based on NOEMA data. Columns 4 and 5: The lower and upper side-band continuum fluxes or  $3\sigma$  upper limits. Column 6: The spectroscopic redshift associated with the line identification. Column 7: The FWHM of the line. Column 8: The velocity-separation between the source and HerBS-70. Columns 9 and 10: The line fluxes and  $3\sigma$  upper limits.

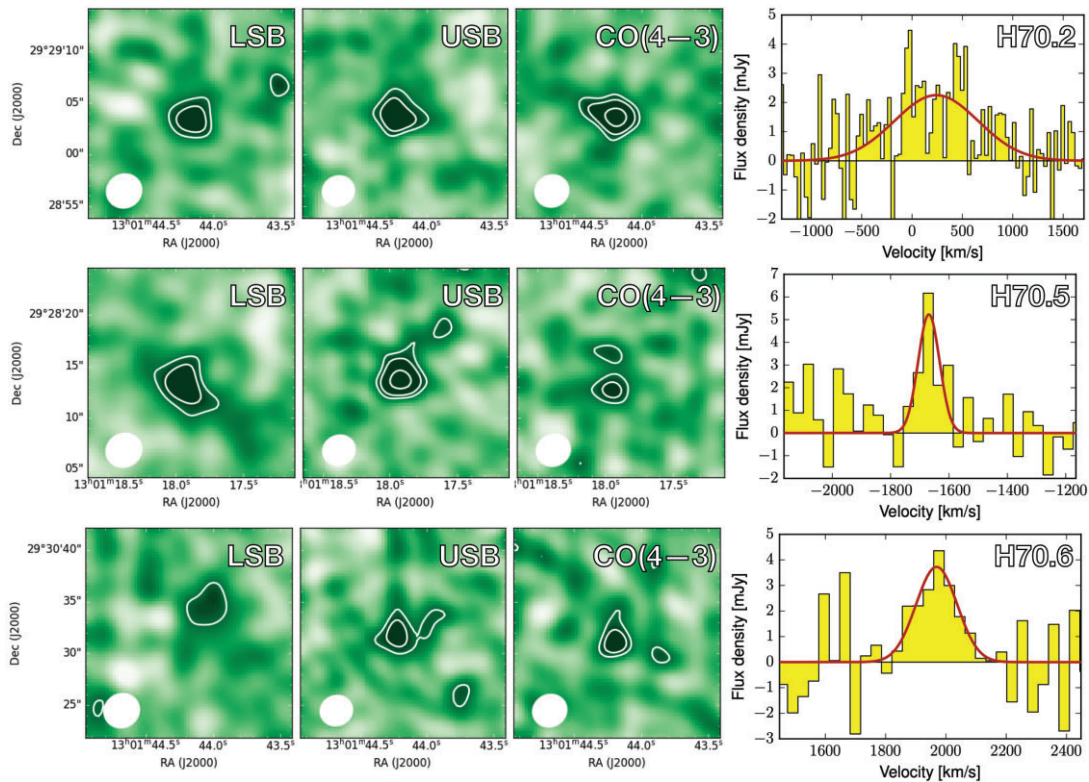


**Figure 7.** The continuum emission, as well as the moment-0 and spectra of the NOEMA observations of the three sources with spectroscopic line detections (H70.2, H70.5, and H70.6; from top to bottom). The poststamps are cut out at 20 by 20 arcsec, and the contours are drawn at 2, 3, and  $5\sigma$ . The bottom left ellipse indicates the beam size. The spectra are shown in 35 km s<sup>-1</sup> bins, and the velocity axis is derived relative to the zero-velocity of HerBS-70E.

between 80 and 500 Myr. These observations seem to suggest that the protocluster system is rapidly processing its available gas, and could move towards a quenched cluster system in the  $z \approx 1$  Universe (Shimakawa et al. 2018).

This low depletion time-scale is also reflected in a comparison to the cosmic molecular gas density. The combined gas mass in H70.2, 0.5, and 0.6 equals a total of  $33 \pm 6 \times 10^{10} M_{\odot}$ . Meanwhile, the cosmic molecular gas density estimate in Decarli et al. (2019) predicts  $\sim 5 \times 10^7 M_{\odot} \text{ Mpc}^{-3}$ . The gas density across the 735 Mpc<sup>3</sup> volume surrounding the HerBS-70 environment probed by these observations is roughly only nine times higher than the average gas density in the  $z = 2.3$  Universe. Although CO(4-3) might not represent the total gas mass in the HerBS-70 system, this could point

to a rapidly quenching system at  $z = 2$ , in line with the evolutionary picture reported in Shimakawa et al. (2018), where clusters move from star forming to quenched in the  $z = 2-3$  Universe as their gas reservoirs deplete.

## 4.2 Continuum overdensity estimates

The SCUBA-2 observations revealed twenty-one  $>3.5\sigma$  dusty sources in the vicinity of HerBS-70 (excluding the central source). Here, we analyse the continuum properties of the SCUBA-2 identified sources, and evaluate the overdensity hypothesis based on these continuum images and multiwavelength continuum data. Although the spectroscopic observations are able to better verify the nature of

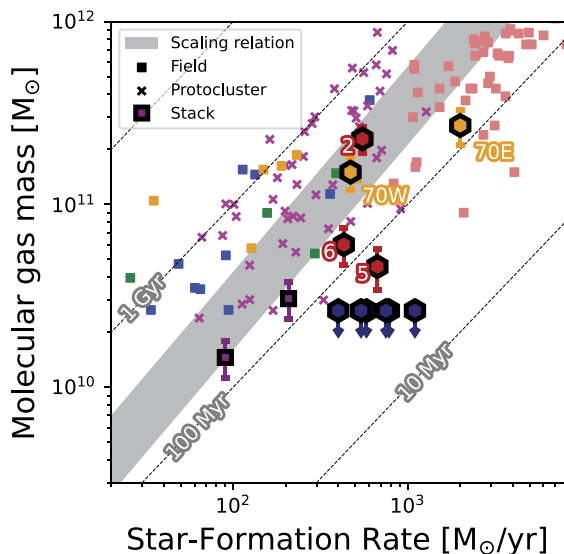


**Figure 8.** The molecular gas mass estimates based on the NOEMA observations for HerBS-70E, W, and the three detected sources (orange and red filled hexagons), as well as the upper limits on the six non-detected galaxies (blue filled hexagons). These are compared against scaling relations from field galaxies (fill and magenta squares Scoville et al. 2016), sub-mm galaxies (pink squares Bendo et al. 2023; Hagimoto et al. 2023), known protoclusters (purple crosses Zavala et al. 2019; Pérez-Martínez et al. 2023), and stacking experiments (big squares Alberts et al. 2021). The NOEMA-identified sources lie below the scaling relation, and the deep NOEMA observations further provide confidence our observations are deep enough to characterize galaxies down to depletion times  $t_{\text{dep}} < 80$  Myr.

these continuum sources, a thorough investigation of the continuum observations can provide context for subsequent sub-mm camera observations that have not yet had the luxury of spectroscopic follow-up.

#### 4.2.1 Infrared photometric redshifts

Eleven sources identified by SCUBA-2 (excluding HerBS-70E&W) have nearby *Herschel* galaxies within one JCMT beam identified through the HELP catalogue (Shirley et al. 2021). This *Herschel* catalogue is produced using source extraction from the 250, 350, and 500  $\mu\text{m}$  maps, and thus includes sources that would have otherwise been too faint to be detected at 250  $\mu\text{m}$  alone, which is standard for the other H-ATLAS catalogues (i.e. Valiante et al. 2016; Furlanetto et al. 2018). Interestingly, in addition to HerBS-70, only three of the six sources detected at  $>5\sigma$  at 850  $\mu\text{m}$  have *Herschel* counterparts (with 5 *Herschel* detections at 250  $\mu\text{m}$  for the 11 SCUBA-2 sources detected at  $>4\sigma$ ). As shown in Fig. A1, the reason for the lack of *Herschel* photometry is either due to nearby bright galaxies that affect the source extraction or because the relatively faint 250  $\mu\text{m}$  flux densities at which the sources are extracted (Valiante et al. 2016), which can be expected for  $z = 2.3$  sources.

For those SCUBA-2 sources without any *Herschel* counterparts, we extract the SPIRE fluxes from the calibrated, background-subtracted images from the second data release of H-ATLAS (Smith et al. 2017).<sup>4</sup> We use the peak SCUBA-2 position, and extract the fluxes at 250, 350, and 500  $\mu\text{m}$  directly from these maps. We use the map-based average noise estimates of 6.1, 5.6, and 6.0 mJy for 250,

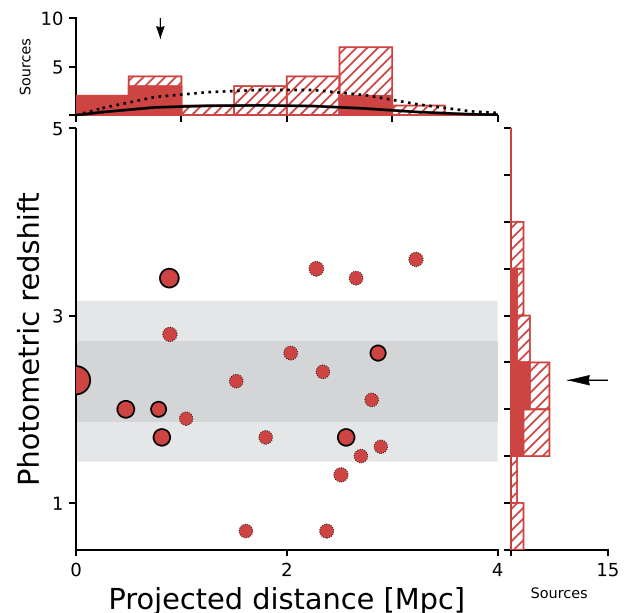


**Figure 9.** The projected distance from the central source (HerBS-70) versus the photometric redshift estimate from a fit of the template in Pearson et al. (2013) shows an excess of  $>5\sigma$  sources within one megaparsec. Larger red dots refer to higher signal-to-noise detections, where sources with a black border have at least SNR greater than 5. The distribution of the photometric redshift estimates of these sources peaks at  $z_{\text{phot}} = 2.5$ , with the filled histograms showing all  $>5\sigma$  sources. The arrow on the right-hand-side histogram indicates the  $z_{\text{spec}} = 2.3$  of HerBS-70, and the arrow along the top histogram shows the expected size of 0.8 Mpc for a protocluster core at  $z = 2$  (Chiang et al. 2017). The grey-filled regions indicate the 1 and  $2\sigma$  uncertainty in the photometric redshift relative to  $z = 2.3$ . The majority of robustly detected ( $5\sigma$ ) sources lie around the photometric redshift of HerBS-70, and fall within the expected size of a protocluster core. The dashed and solid lines in the top histogram show the expected distribution of sources based on the number counts from Simpson et al. (2019). A sizeable fraction of sources lie close to HerBS-70, suggesting an overdensity of 3.5 times the number of sources expected for field galaxies.

350, and 500  $\mu\text{m}$ , respectively. We note the possibility of a boosted 500  $\mu\text{m}$  flux due to the bright [C II] emission line at an observed wavelength of  $\sim 520$   $\mu\text{m}$  (Smail et al. 2011; Seymour et al. 2012; Dannerbauer et al. 2014). This effect would boost the photometric redshift estimates of the sources, although the expected deviation would depend on the interstellar medium properties of each galaxy, and are hard to quantify without dedicated observations (Burgarella et al. 2022).

We fit the FIR fluxes from both the *Herschel* and SCUBA-2 photometry, using a two-temperature modified black-body from Pearson et al. (2013). This template is suitable, since it was derived from *Herschel* photometry for 40 galaxies at low and high redshift. Fig. 9 shows the resulting redshift distribution for all 22 sources (incl. HerBS-70EW) identified by SCUBA-2 as a function of their projected distance to the central HerBS-70 position. The distribution of photometric redshift estimates lie around  $z_{\text{phot}} = 2.5$ , which encompasses the spectroscopic redshift of HerBS-70 ( $z = 2.3$ , horizontal arrow). We note that this is not necessarily an indication of an overdensity, as the typical redshift distribution for *Herschel*- and SCUBA-2 extracted sources is around  $\bar{z} = 2.5 \pm 0.5$  (Birkin et al. 2021). Previous studies have shown that the average uncertainty in a photometric redshift estimate is roughly  $\Delta z = 0.13(1 + z)$  (Pearson et al. 2013; Ivison et al. 2016; Bakx et al. 2018). As an extra

<sup>4</sup><https://www.h-atlas.org/public-data/download>



check, we also compute the photometric redshifts using the method described in Ivison et al. (2016), and find broad agreement between the photometric redshift estimates. We show the fitted spectra and poststamps of the six  $>5\sigma$  sources in Fig. A1.

While the photometric redshift distribution of SCUBA-2 sources is unable to identify an overdensity of sources, the projected distance between each SCUBA-2 source and HerBS-70 suggests a marginal overdensity. The top histogram in Fig. 9 shows the distance distribution of sources, where the observed number of sources (filled and hatched for 5 and  $3.5\sigma$  sources, resp.) lie substantially above the predicted number of sources (solid and dashed lines for 5 and  $3.5\sigma$  sources, respectively). The predicted number of sources are calculated based on the number counts from Simpson et al. (2019). For each pixel in the noise map, we calculate the expected number of sources above 3.5 and  $5\sigma$  as a function of the radial distance. We indicate the expected size of the protocluster core ( $r = 0.8$  Mpc; Chiang et al. 2017) with a vertical arrow. At the shorter distances, the number of  $5\sigma$  sources is in noticeably above the expected number of sources. At longer distances, the number of  $3.5\sigma$  sources appears to exceed the expected number of sources, although this could be inflated by the number of *false positives*.

#### 4.2.2 Source counts

We calculate the number counts,  $N(> S')$ , by counting the number of sources above a certain deboosted flux  $S'$  across the area,  $A$ , in which they would be detected. We account for the non-flat noise profile, and calculate the area where we would be able to detect sources at a given flux above  $3\sigma$ . We account for the false-positive ( $FP$ ; contamination) and false-negative ( $FN$ ; completeness) rates using

$$N(> S') = \sum_{S_i > S'} \frac{FP}{FN \times A}. \quad (1)$$

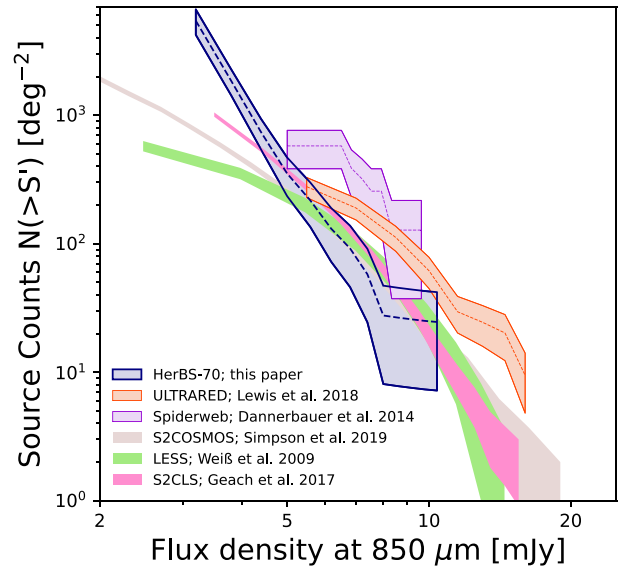
The noise estimates on the source counts are proportional to the square root of the number of sources contributing to the source count estimate, where the fluxes are accounted for Eddington boosting.

Fig. 10 shows the source counts of the HerBS-70 SCUBA-2 observations against field surveys (Weiß et al. 2009; Casey et al. 2013; Geach et al. 2017; Simpson et al. 2019) and known protocluster systems (Dannerbauer et al. 2014; Lewis et al. 2018). The central source is masked similar to other studies (e.g. Lewis et al. 2018) and, thus the deep observations provide secure estimates of the source counts from roughly 10 mJy down to  $\sim 2.5$  mJy.

The source counts for the region around HerBS-70 are comparable with field galaxies over the majority of the flux density regime. The faint end of the source counts appears to diverge from all models, due to the deep observations and the shrinking area where our observations probe below 3 mJy. The bright end of the source counts is in line with the behaviour seen for moderately overdense regions such as the ones seen in Lewis et al. (2018) and Lacaille et al. (2019), who also struggle to find evidence for overdensities in the source counts alone. While our analysis on particular regions in the SCUBA-2 map indicated strong overdensities (e.g. a factor of 2.9 seen in the centre of Fig. 2; see Section 4.2.3), such details appear to be averaged out across the wider map as suggested by the source counts (c.f., Zhang et al. 2022).

#### 4.2.3 An overdensity of continuum sources

As shown in the previous subsections, the photometric redshifts and source counts derived from the 850  $\mu$ m continuum map together



**Figure 10.** The source counts at 850  $\mu$ m show the number of sources above the normalized flux per square degree. The source counts are compared against field surveys (Weiß et al. 2009; Casey et al. 2013; Geach et al. 2017; Simpson et al. 2019) and known protocluster systems (Dannerbauer et al. 2014; Lewis et al. 2018, shown with rimmed fill). The source counts of HerBS-70 are in line with the bulk of field galaxies at flux densities from 4 to 10 mJy, and suggest moderate overdensity at the faint- and bright ends of the source counts. As previously found in Lewis et al. (2018), source counts struggle to identify overdense regions, and we suggest instead using spatially resolved studies to look for cosmic overdensities.

with additional continuum data do not indicate clear evidence for an overdensity in the wide Mpc-scale environment around HerBS-70. However, as shown in Fig. 9, there is an indication of a source overdensity in the centre of the HerBS-70 field. We estimate the overdensity of sources close to HerBS-70 based on a direct comparison to the source counts from Geach et al. (2017), and we visualize that using blue contours in Fig. 2. We generate these contours for galaxies detected above  $5\sigma$  using a method that compares the expected number of sources against the actually observed distribution of sources, smoothed by a kernel on the size of the typical protocluster core (Chiang et al. 2017).

We calculate the expected number of sources using the following method. We use the noise map to calculate the  $5\sigma$  flux limit for each individual pixel, and use the source count model from Geach et al. (2017) to calculate the per-pixel expected number of sources (a value much smaller than 1). These are the ‘expected background’ against which we observe the true detected sources. Since these are the ‘expected’ number of sources, we reflect them as negative values, and for each source identified above  $5\sigma$ , we replace the index by a value with a 1 (since one source was actually observed at this single pixel). Note that we exclude the central source HerBS-70EW from this calculation. We then smooth the resulting image down to the scale of a typical overdensity (here we take a Gaussian kernel with a characteristic width,  $\sigma$ , of 1 arcminute (500 kpc), or an FWHM of 1.2 Mpc, roughly matching the expected size of a protocluster core at  $z = 2$  (Chiang et al. 2013). As seen in Fig. 2, the central region appears to be overdense by a factor of  $\delta_{\text{bias}} = 2.9$ .

This region features three  $>5\sigma$  sources on top of the HerBS-70 system, and as shown in previous research (Lacaille et al. 2019), these low-number statistics result in a high uncertainty on the bias. We



estimate the uncertainty in the bias by repeatedly re-drawing from our  $>5\sigma$  sample, and calculating the bias value within 1 Mpc of HerBS-70. The resulting bias is  $\delta_{\text{bias}} = 3.4 \pm 1.3$ . We compare this estimate against known bright sources from fields without obvious sub-mm overdensities. This is important, since sub-mm galaxies are known to cluster together, even if they are not associated to a protocluster system. In this case, we use the UDS field from the COSMOS Legacy Survey (Geach et al. 2017) as a comparison field, similar to previous protocluster studies (Lacaille et al. 2019). We examine the spatial distribution of  $>5\sigma$  sources ( $N = 335$ ) in the 50 arcminute diameter UDS field by redrawing this selection, and calculate the observed bias in the environment around a randomly chosen  $>5\sigma$  source. This central source is subsequently masked – same as with our HerBS-70EW analysis – and the peak bias within 1 Mpc is then evaluated. The average bias is  $\delta_{\text{bias}} = 0.7 \pm 2.2$ . As a sanity check, we find that the average bias across the entire 50 arcminute diameter UDS field is  $\delta_{\text{bias}} = 0.0 \pm 1.5$ . The mean of zero is reasonable<sup>5</sup>, since we derived the expected number of sources from the Geach et al. (2017) source counts. Similarly, the fact that the typical bias is around 1 is in line with two-point correlation studies for sub-mm sources, which find a typical spatial association of  $w(\omega = 1') = 1$  (Amvrosiadis et al. 2019). If we directly compare a random draw of the UDS against a resampled HerBS-70 field, we find a higher bias in HerBS-70 for 90 per cent of all draws. Similar to the relatively poor statistics of previous continuum camera studies (e.g. Lewis et al. 2018), we find a tentative indication for a HerBS-70 overdensity, however note that a selection effect (i.e. spatial clustering of bright sub-mm sources) cannot be ruled out on continuum data alone (e.g. Chen et al. 2023).

Evaluating the bias of HerBS-70, particularly the inner 1 Mpc shows a strong overdensity relative to the field (Simpson et al. 2019), as seen in Figs 2 and 9. This suggests that at some of the  $5\sigma$  detected galaxies could be true protocluster core members. The overdensity bias changes with the size of the smoothing kernel, with tests at smaller and larger kernels resulting in smaller biases. This agrees with the distribution of the projected distances, which also suggests that the potential HerBS-70 system would be  $\sim 1$  Mpc in size, and lines up with models and past observations. For example, Chiang et al. (2017) show that while protoclusters collapse to form dense environments with cosmic time, the cores of protoclusters grow in size. Studies at higher redshift (e.g. Oteo et al. 2018; Long et al. 2020; Remus et al. 2022 at  $z = 4$ ) that find smaller protocluster cores on the order of  $\sim 300$  kpc, while environments at the peak of cosmic star formation (Madau & Dickinson 2014) extend over larger areas, similar to the  $\sim 1.2$  Mpc size suggested by our experiment, and the 0.8 Mpc size predicted by Chiang et al. (2017) at  $z = 2$ .

#### 4.2.4 The large-scale environment around HerBS-70

In an effort to explore the larger-area surroundings of HerBS-70 where most of the protocluster environment should be located (Chiang et al. 2017), we compare against the catalogue of WISE sources<sup>6</sup> from the WISE All-Sky catalogue (Wright et al. 2010; Cutri & et al. 2012) with 30 arcmin around HerBS-70, and compare the positions against data from the recent LOFAR release (van Haarlem et al. 2013; Shimwell et al. 2022). The WISE sources will likely be sensitive to ordinary, massive galaxies at lower redshifts, while the 150 MHz LOFAR data is sensitive to radio-bright galaxies

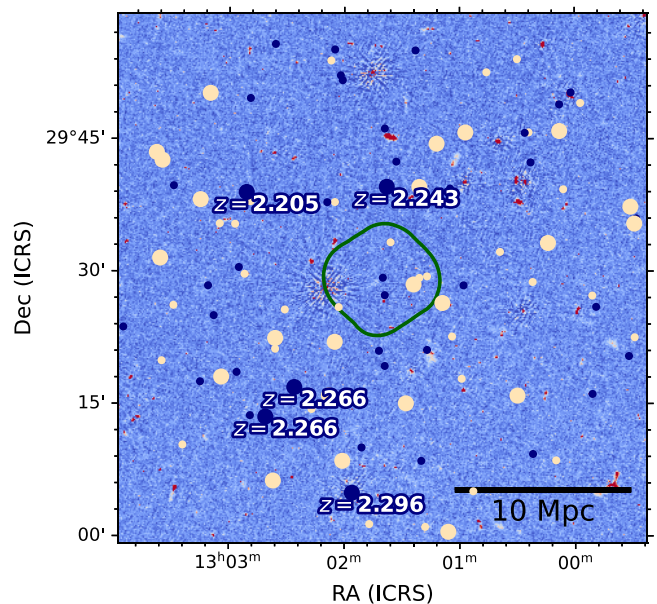


**Figure 11.** The spatial distribution of WISE-detected sources which are shown relative to the observed SCUBA-2 map (green contour), with the LOFAR image on the background (Shimwell et al. 2022). Sources with photometric ( $\Delta z = 0.5$ ; small marker) and spectroscopic redshifts ( $\Delta z = 0.1$ ;  $\pm 5000$  km s<sup>-1</sup>; large marker) close to the spectroscopic redshift of HerBS-70 ( $z = 2.31$ ) are shown in blue, and sources outside of this redshift window are shown in light orange. Five quasars with spectroscopic redshifts within the region of HerBS-70 are seen out to distances of  $\sim 13$  Mpc, which is around the expected size of an overdensity based on both  $N$ -body simulations and semi-analytical models discussed in Chiang et al. (2017). The green contours show the extent of the SCUBA-2 observations where the per-beam source sensitivity is 2 mJy. These sources are important for follow-up observations, as they could play a role on the large-scale environment around HerBS-70, although currently not enough evidence exists to identify these sources as part of a cosmic overdensity.

and quasars.<sup>7</sup> The LOFAR sensitivity is better than  $0.1$  mJy beam<sup>-1</sup> at  $\sim 6$  arcsec resolution. The blue points in Fig. 11 mark galaxies and quasars within  $\Delta z = 0.25$  for photometric redshifts (small points) and  $0.05$  for spectroscopic redshifts (large points, equivalent to  $\pm 5000$  km s<sup>-1</sup>). A bright source to the east of HerBS-70 has been masked out, although some radially extending artefacts still remain in the image that could affect sources in the eastern side of the SCUBA-2 map. Sources outside of these redshift windows are shown in light orange. Five quasars with known spectroscopic redshifts (Berger & Fringant 1977; Richards et al. 2009, 2015; Pâris et al. 2018) are seen out to projected distances of  $\sim 13$  Mpc from HerBS-70, which is around the expected size of an overdensity based on both  $N$ -body simulations and semi-analytical models at  $z = 2$ , as discussed in Chiang et al. (2017). Currently, not enough information is available on these quasars to identify an overdensity, however follow-up of these sources might help identify the large-scale environment around the HerBS-70 system. These bright sources at larger separation could further help identify additional evolutionary pathways of quenching of star formation, as a widespread triggering of AGN is not uncommon for protocluster environments (e.g. Casey 2016).

<sup>5</sup>Note that the uncertainty is not the uncertainty on the mean, but instead the field-to-field variation.

<sup>6</sup>[https://wise2.ipac.caltech.edu/docs/release/allsky/expsup/sec1\\_4b.html](https://wise2.ipac.caltech.edu/docs/release/allsky/expsup/sec1_4b.html)

<sup>7</sup>The LOFAR maps are produced following the method described in Sweijen et al. (2022), using the image archive at [https://lofar-surveys.org/dr1\\_release.html](https://lofar-surveys.org/dr1_release.html).

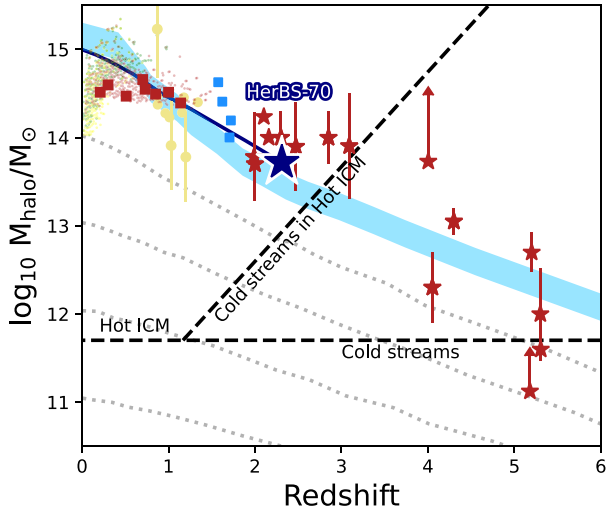


**Figure 12.** The halo mass distribution of HerBS-70 (blue star) is shown against various samples of clusters and models of the evolution of clusters with redshift. Red stars refer to cluster-masses derived from sub-mm camera observations (Steidel et al. 1998; Kurk et al. 2000; Blain et al. 2004; Chapman et al. 2009; Daddi et al. 2009; Lehmer et al. 2009; Tamura et al. 2009; Capak et al. 2011; Kuiper et al. 2011; Walter et al. 2012; Hodge et al. 2013; Dannerbauer et al. 2014; Yuan et al. 2014; Casey et al. 2015; Chiang et al. 2015; Diener et al. 2015; Umehata et al. 2015; Casey 2016; Miller et al. 2018; Lacaille et al. 2019; Smith et al. 2019b; Hill et al. 2020; Long et al. 2020; Calvi et al. 2021; Guaita et al. 2022). The yellow circles at  $z = 1$  are from the GCLASS survey (van der Burg et al. 2014), and the blue squares represent high-redshift virialized clusters (Stanford et al. 2012; Zeimann et al. 2012; Mantz et al. 2014; Newman et al. 2014). At the  $z < 1.5$  Universe, we represent the vast samples of local clusters (pink points) compiled by Bleem et al. (2015) and references therein using red squares for clusters from SPT, green pixels for clusters from Planck, and using yellow pixels for clusters from the ACT. The scaling relations (dashed lines) are from the Millennium I and II simulations (McBride, Fakhouri & Ma 2009; Fakhouri & Ma 2010) shown at present-day masses of  $10^{11}$ – $10^{14} M_{\odot}$ . We scale the evolution of the most massive halo to the  $z = 2.3$  mass of HerBS-70 to forward model the cluster redshift into the present age (blue line), finding a total mass on the order of  $\sim 1 \times 10^{15} M_{\odot}$ . The filled blue region represents the evolution of the most massive cluster (+ errors) from Chiang et al. (2013). The thick dashed black lines indicate the redshift-halo mass regions where the mechanics of gas inflow and the cooling mechanisms of galaxy clusters transition (Dekel & Birnboim 2006; Overzier 2016). This causes the subsequent quenching of galaxy clusters into local sources (Shimakawa et al. 2018).

#### 4.3 Cosmological evolution of the HerBS-70 halo

Fig. 12 shows the evolutionary pathway of the HerBS-70 system compared to known clusters and protoclusters and evolutionary models. High-redshift cluster mass estimates offer a cursory glimpse at the potential evolutionary track of systems in the early Universe, although they are dependent on multiple assumptions and scaling relations, which results in near-order of magnitude uncertainties in the halo mass estimates. In this case, we use the conservative limits of the scaling relations, in order to not overestimate the cluster mass, although future observations should focus on improving the robustness of these estimates through spectroscopic confirmation of the members of the HerBS-70 system.

We derive the halo mass of HerBS-70 from the dust mass estimates for sources in the protocluster core (i.e. HerBS-70E & W, and sources H70.2 and H70.6), since the SCUBA-2 observations are sensitive to the most dusty, star-forming galaxies. We focus on just the central core, since our SCUBA-2 observations have provided the

best constraints on the protocluster core, and the statistics of the overdensity are averaged out towards larger scales. The combined dust masses of all sources identified in Table 2 add to  $8.3 \times 10^9 M_{\odot}$ . We then assume a gas-to-dust ratio of 100 to acquire a total gas mass estimate (Hagimoto et al. 2023).<sup>8</sup> Particularly, this value has a moderate evolution with redshift (see Péroux & Howk 2020 for a discussion) and represents solar metallicity systems (Pantoni et al. 2019; De Looze et al. 2020; Graziani et al. 2020; Millard et al. 2020), which could be a relatively good tracer of even the high-redshift Universe (Vijayan et al. 2019; Litke et al. 2022; Popping & Péroux 2022). Cluster evolution models (Chiang et al. 2013) suggest that 30 per cent of the mass of the cluster is contained within the inner 0.8 Mpc, and we assume a fixed baryonic-to-dark matter fraction of 5 per cent (Behroozi & Silk 2018). Based on these assumptions, the estimated total cluster mass is  $6 \times 10^{13} M_{\odot}$ .

The evolution models from McBride et al. (2009) and Fakhouri & Ma (2010) predict a future halo mass in excess of  $10^{15} M_{\odot}$ . Although the models are derived for different halo masses, the evolution between them is only minor, and we thus feel comfortable to scale the most massive model to the estimated halo mass of  $5 \times 10^{13} M_{\odot}$  at  $z = 2.3$ . The halo mass is on par with massive local passive galaxy clusters such as the  $\sim 10^{15} M_{\odot}$  Virgo cluster (Fouqué et al. 2001), and the HerBS-70 system might thus represent the central quenching phase in one of the most massive galaxy clusters in the Universe. Here we do well to stress that direct extrapolations of the cluster masses from dust and gas-mass estimates is prone to large errors in the final mass estimate, as well as depends on ad hoc assumptions on the content of dusty galaxies in protoclusters. Future work could better estimate the halo mass using complementary methods, such as the abundance matching technique discussed in Long et al. (2020); Calvi et al. (2021) that requires deep optical imaging, as well as better comparison to models of cosmological overdensities (e.g. Chiang et al. 2017).

This short expected lifetime ( $\leq 70$  Myr) is consistent with the hierarchical picture of massive galaxy formation (Hopkins et al. 2008), which might be further exacerbated by the internal AGN (e.g. Ito et al. 2022; Mountrichas et al. 2022). The sudden lack of gas feeding from the environment (e.g. Shimakawa et al. 2018 for an evolutionary picture) suggests the future evolution of the central HerBS-70 source is likely to lead to a massive red-and-dead giant elliptical galaxy by  $z = 0$  (Toft et al. 2014; Ikarashi et al. 2015; Simpson et al. 2017; Stach et al. 2017). The findings reported in this paper add to the growing evidence towards this hierarchical pathway of DSFGs to quenched elliptical galaxies given the high stellar masses (Hainline et al. 2011; Aravena et al. 2016b), high specific SFRs (Straatman et al. 2014; Spilker et al. 2016; Glazebrook et al. 2017; Schreiber et al. 2018; Merlin et al. 2019) and location in an overdense region (Blain et al. 2004; Weiß et al. 2009; Hickox et al. 2012).

#### 4.4 Finding protoclusters among multiple-DSFG systems

Large area surveys such as the ones done with the Atacama Cosmology Telescope, *Herschel*, *Planck*, and the South Pole Telescope are able to select the apparently brightest DSFGs in the sky. Because the bright end of the luminosity function is steep, instead of finding the intrinsically brightest galaxies, these surveys have found large

<sup>8</sup>This approach is in line with the sum of the gas mass found in Section 4.1, and should better account for the total gas mass instead of just the molecular gas mass.

numbers of gravitationally lensed (Treu 2010), less luminous galaxies (Negrello et al. 2010; Busmann et al. 2013; Vieira et al. 2013; Busmann et al. 2015; Spilker et al. 2016; Negrello et al. 2017).

As surveys move towards lower brightness sources, the fraction of unlensed sources increases (Cai et al. 2013; Busmann et al. 2015; Bakx, Eales & Amvrosiadis 2020a; Bakx et al. 2024). Follow-up observations with mm/submm interferometers (NOEMA and ALMA) have resolved these DSFGs revealing, in a few cases, multiple sources at the same redshift (Hodge et al. 2013; Karim et al. 2013; Zavala et al. 2015; Scudder et al. 2016; Oteo et al. 2018; Neri et al. 2020). However, such systems remain rare with, for instance, two binary systems found in 13 sources studied in Neri et al. (2020) – including HerBS-70 – and 8 out of 62 in the spectroscopic survey by Urquhart et al. (2022), i.e. 15 and 13 per cent, respectively (see also Gómez-Guijarro et al. 2019). Multiple systems at high-redshift are prime targets to identify dusty protoclusters and recent surveys such as *z*-GAL (Cox et al. 2023) have doubled the numbers of high-*z* sources displaying genuine multiplicity, beyond what is expected from field galaxies (Bakx et al. in preparation). Here, we note that identifying and studying groups of sources at  $z > 3.5$  is of crucial importance to test the  $\Lambda$ CDM paradigm (Harrison & Hotchkiss 2013).

As shown in this study, the case of HerBS-70 at  $z = 2.3$  presents a clear case of multiplicity with an overdensity of sub-mm sources. This indicates that this binary system, identified with NOEMA, lies at the core of a massive protocluster. The likely quenching ongoing in the central source HerBS-70E could further be studied by, for example, absorption line studies, that are able to probe the gas cycle (Spilker et al. 2018, 2020a, b; Berta et al. 2021; Butler et al. 2021), and differentiate between the effect of the AGN and star formation feedback. Finally, at  $z = 2.3$ , this source is an excellent target for narrow-band observations that aim for H $\alpha$  emission using near-infrared facilities (e.g. Subaru, VLT, Keck and Gemini; Kurk et al. 2000; Koyama et al. 2013, 2021). These could also measure independently the redshifts of the bright sub-mm sources, and provide several tens of fainter protocluster components that are missed in current sub-mm imaging surveys.

## 5 CONCLUSIONS

We have presented (i) the 850  $\mu$ m SCUBA-2 imaging of the field around HerBS-70, a binary system of bright DSFGs at  $z = 2.3$ , and (ii) subsequent NOEMA observations of the nine brightest SCUBA-2 targets surrounding HerBS-70 aimed to test the protocluster hypothesis. Three of these nine targeted SCUBA-2 sources were found to be at the same redshift as HerBS-70, and the remaining six are excluded from the protocluster environment. These observations, and existing multiwavelength data, allow us to conclude the following:

- (i) HerBS-70 is located at the centre of a candidate protocluster core ( $\sim 0.8$  Mpc) with a volume density  $\sim 36$  times higher than field galaxies, based on NOEMA spectroscopic observations. These observations targeted the brightest nine continuum galaxies in the HerBS-70 environment with a surface density estimates  $\sim 3$  higher than field galaxies based on the SCUBA-2 sub-mm continuum map.
- (ii) Meanwhile, the continuum overdensity estimates based on number counts and across the wider continuum map do not provide evidence towards the overdensity hypothesis, indicating the limits of continuum observations in identifying overdensities.
- (iii) The depletion time-scales of HerBS-70E, 70W, H70.2, H70.5, and H70.6 are around 500–100 Myr, indicating there is rapid gas

depletion, which will likely result in the rapid quenching of the environment.

- (iv) Forward-modelling of the dust-based halo mass estimate ( $\approx 5 \times 10^{13} M_{\odot}$ ) suggests a present-day halo mass of  $1 \times 10^{15} M_{\odot}$ , in excess of the local, massive Virgo cluster, although we note that this method is prone to biases and large errors.

The SCUBA-2 map and subsequent NOEMA follow-up have revealed and verified an overdensity of dusty sources around HerBS-70. The  $z = 2.3$  redshift of this source makes it an excellent candidate for H  $\alpha$  narrow-band follow-up (e.g. Koyama et al. 2021), in order to reveal the more numerous, but less dusty components of the HerBS-70 system. Increasing the number of protocluster components can then provide insights into the structure and properties of more normal galaxies within the HerBS-70 system.

The advent of large spectroscopic samples of DSFGs (including sizeable numbers of multiple sources) further entice similar sub-mm camera studies, particularly in light of the production of improved mm/sub-mm cameras, such as NIKA2 (Catalano et al. 2018), TolTEC (Wilson et al. 2020), and SCUBA-3<sup>9</sup>. Such observational studies will enable to better constrain and understand the properties and evolution of protoclusters and in the early Universe, in particular at the peak of cosmic evolution.

## ACKNOWLEDGEMENTS

The authors kindly thank the anonymous referee for their comprehensive comments that significantly improved the scientific scope of this manuscript. Financial support from the Knut and Alice Wallenberg foundation is gratefully acknowledged through grant no. KAW 2020.0081. TB, MH, and YT acknowledge funding from NAOJ ALMA Scientific Research Grant Number 2018–09B and JSPS KAKENHI Numbers 17H06130, 22H04939, and 22J21948. The JCMT is operated by the East Asian Observatory on behalf of The National Astronomical Observatory of Japan; Academia Sinica Institute of Astronomy and Astrophysics; the Korea Astronomy and Space Science Institute; the National Astronomical Research Institute of Thailand; Center for Astronomical Mega-Science (as well as the National Key R&D Program of China with No. 2017YFA0402700). Additional funding support is provided by the Science and Technology Facilities Council of the United Kingdom and participating universities and organizations in the United Kingdom and Canada. Additional funds for the construction of SCUBA-2 were provided by the Canada Foundation for Innovation. SS was partly supported by the ESCAPE project; ESCAPE – The European Science Cluster of Astronomy and Particle Physics ESFRI Research Infrastructures has received funding from the European Union’s Horizon 2020 research and innovation programme under Grant Agreement No. 824064. SS also thanks the Science and Technology Facilities Council for financial support under grant ST/P000584/1. SU would like to thank the Open University School of Physical Sciences for supporting this work. HD acknowledges financial support from the Agencia Estatal de Investigación del Ministerio de Ciencia e Innovación (AEI-MCINN) under grant (La evolución de los cúmulos de galaxias desde el amanecer hasta el mediodía cósmico) with reference (PID2019-105776GB-I00/DOI:10.13039/501100011033) and acknowledge support from the ACISI, Consejería de Economía, Conocimiento y Empleo del Gobierno de Canarias and the European Regional Development Fund

<sup>9</sup><https://www.eaoobservatory.org/jcmt/wp-content/uploads/sites/2/2019/10/Guide-to-the-new-850um-MKID-camera-performance.pdf>



(ERDF) under grant with reference PROID2020010107. This work benefited from the support of the project Z-GAL ANR-AAPG2019 of the French National Research Agency (ANR). LOFAR data products were provided by the LOFAR Surveys Key Science project (LSKSP; <https://lofar-surveys.org/>) and were derived from observations with the International LOFAR Telescope (ILT). LOFAR (van Haarlem et al. 2013) is the Low Frequency Array designed and constructed by ASTRON. It has observing, data processing, and data storage facilities in several countries, which are owned by various parties (each with their own funding sources), and which are collectively operated by the ILT foundation under a joint scientific policy. The efforts of the LSKSP have benefited from funding from the European Research Council, NOVA, NWO, CNRS-INSU, the SURF Co-operative, the UK Science and Technology Funding Council and the Jülich Supercomputing Centre. AN acknowledges support from the Narodowe Centrum Nauki (NCN), Poland, through the SONATA BIS grant UMO-2020/38/E/ST9/00077.

## DATA AVAILABILITY

The data underlying this article will be shared on reasonable request to the corresponding author.

## REFERENCES

- Alberts S. et al., 2021, *MNRAS*, 501, 1970
- Algera H. S. B. et al., 2023, *MNRAS*, 518, 6142
- Amvrosiadis A. et al., 2019, *MNRAS*, 483, 4649
- Aravena M., Younger J. D., Fazio G. G., Gurwell M., Espada D., Bertoldi F., Capak P., Wilner D., 2010, *ApJ*, 719, L15
- Aravena M. et al., 2016a, *MNRAS*, 457, 4406
- Aravena M. et al., 2016b, *ApJ*, 833, 68
- Bañados E., Venemans B., Walter F., Kurk J., Overzier R., Ouchi M., 2013, *ApJ*, 773, 178
- Bakx T. J. L. C. et al., 2018, *MNRAS*, 473, 1751
- Bakx T. J. L. C., Eales S., Amvrosiadis A., 2020a, *MNRAS*, 493, 4276
- Bakx T. J. L. C. et al., 2020b, *MNRAS*, 494, 10
- Bakx T. J. L. C. et al., 2020c, *MNRAS*, 496, 2372
- Bakx T. J. L. C., Gray B. S., González-Nuevo J., Bonavera L., Amvrosiadis A., Eales S., Hagimoto M., Serjeant S., 2024, *MNRAS*, 527, 8865
- Banerji M., Chapman S. C., Smail I., Alaghband-Zadeh S., Swinbank A. M., Dunlop J. S., Ivison R. J., Blain A. W., 2011, *MNRAS*, 418, 1071
- Behroozi P., Silk J., 2018, *MNRAS*, 477, 5382
- Bendo G. J. et al., 2023, *MNRAS*, 522, 2995
- Berger J., Fringant A. M., 1977, *A&AS*, 28, 123
- Berta S. et al., 2013, *A&A*, 551, A100
- Berta S. et al., 2021, *A&A*, 646, A122
- Berta S. et al., 2023, *A&A*, 678, A28
- Biffi V., Planelles S., Borgani S., Rasia E., Murante G., Fabjan D., Gaspari M., 2018, *MNRAS*, 476, 2689
- Birkin J. E. et al., 2021, *MNRAS*, 501, 3926
- Blain A. W., 1999, *MNRAS*, 309, 955
- Blain A. W., Smail I., Ivison R. J., Kneib J. P., Frayer D. T., 2002, *Phys. Rep.*, 369, 111
- Blain A. W., Chapman S. C., Smail I., Ivison R., 2004, *ApJ*, 611, 725
- Bleem L. E. et al., 2015, *ApJS*, 216, 27
- Borys C., Chapman S., Halpern M., Scott D., 2003, *MNRAS*, 344, 385
- Bruzual G., Charlot S., 2003, *MNRAS*, 344, 1000
- Burgarella D. et al., 2022, *A&A*, 671, A123
- Bussmann R. S. et al., 2013, *ApJ*, 779, 25
- Bussmann R. S. et al., 2015, *ApJ*, 812, 43
- Butler K. M. et al., 2021, *ApJ*, 919, 5
- Cañameras R. et al., 2018, *A&A*, 620, A61
- Cai Z.-Y. et al., 2013, *ApJ*, 768, 21
- Calvi R., Dannerbauer H., Arrabal Haro P., Rodríguez Espinosa J. M., Muñoz-Tuñón C., Pérez González P. G., Geier S., 2021, *MNRAS*, 502, 4558
- Capak P. L. et al., 2011, *Nature*, 470, 233
- Casey C. M., 2016, *ApJ*, 824, 36
- Casey C. M. et al., 2013, *MNRAS*, 436, 1919
- Casey C. M., Narayanan D., Cooray A., 2014, *Phys. Rep.*, 541, 45
- Casey C. M. et al., 2015, *ApJ*, 808, L33
- Castignani G. et al., 2020, *A&A*, 640, A64
- Catalano A. et al., 2018, *J. Low Temp. Phys.*, 193, 916
- Chabrier G., 2003, *PASP*, 115, 763
- Champagne J. B. et al., 2018, *ApJ*, 867, 153
- Chapin E. L., Berry D. S., Gibb A. G., Jenness T., Scott D., Tilanus R. P. J., Economou F., Holland W. S., 2013, *MNRAS*, 430, 2545
- Chapman S. C., Blain A., Ivison R. J., Smail I., Morrison G., 2009, *ApJ*, 691, 560
- Chen J. et al., 2023, *A&A*, 675, L10
- Chiang Y.-K., Overzier R., Gebhardt K., 2013, *ApJ*, 779, 127
- Chiang Y.-K. et al., 2015, *ApJ*, 808, 37
- Chiang Y.-K., Overzier R. A., Gebhardt K., Henriques B., 2017, *ApJ*, 844, L23
- Contini E., De Lucia G., Hatch N., Borgani S., Kang X., 2016, *MNRAS*, 456, 1924
- Coppin K. et al., 2006, *MNRAS*, 372, 1621
- Cowie L. L., Barger A. J., Kneib J. P., 2002, *AJ*, 123, 2197
- Cox P. et al., 2023, *A&A*, 678, A26
- Cutri R. M. et al., 2012, VizieR Online Data Catalog, p. II/311. Available at: <https://ui.adsabs.harvard.edu/abs/2012yCat.2311....0C/abstract>
- Daddi E. et al., 2009, *ApJ*, 694, 1517
- da Cunha E., Charlot S., Elbaz D., 2008, *MNRAS*, 388, 1595
- Dannerbauer H. et al., 2014, *A&A*, 570, A55
- De Breuck C. et al., 2004, *A&A*, 424, 1
- De Looze I. et al., 2020, *MNRAS*, 496, 3668
- Decarli R. et al., 2019, *ApJ*, 882, 138
- Dekel A., Birnboim Y., 2006, *MNRAS*, 368, 2
- Delhaize J. et al., 2017, *A&A*, 602, A4
- Dempsey J. T. et al., 2013, *MNRAS*, 430, 2534
- Di Mascolo L. et al., 2021, *A&A*, 650, A153
- Diener C. et al., 2015, *ApJ*, 802, 31
- Draine B. T., 2003, *ARA&A*, 41, 241
- Draine B. T., Li A., 2007, *ApJ*, 657, 810
- Dressler A., 1980, *ApJ*, 236, 351
- Dunne L., Maddox S. J., Vlahakis C., Gomez H. L., 2021, *MNRAS*, 501, 2573
- Dunne L., Maddox S. J., Papadopoulos P. P., Ivison R. J., Gomez H. L., 2022, *MNRAS*, 517, 962
- Eales S., Lilly S., Webb T., Dunne L., Gear W., Clements D., Yun M., 2000, *AJ*, 120, 2244
- Eales S. et al., 2010, *PASP*, 122, 499
- Emonts B. H. C. et al., 2016, *Science*, 354, 1128
- Emonts B. H. C. et al., 2018, *MNRAS*, 477, L60
- Fakhouri O., Ma C.-P., 2010, *MNRAS*, 401, 2245
- Feltre A., Hatziminaoglou E., Fritz J., Franceschini A., 2012, *MNRAS*, 426, 120
- Feltre A. et al., 2013, *MNRAS*, 434, 2426
- Finner K., James Jee M., Webb T., Wilson G., Perlmutter S., Muzzin A., Hlavacek-Larrondo J., 2020, *ApJ*, 893, 10
- Fouqué P., Solanes J. M., Sanchis T., Balkowski C., 2001, *A&A*, 375, 770
- Fritz J., Franceschini A., Hatziminaoglou E., 2006, *MNRAS*, 366, 767
- Furlanetto C. et al., 2018, *MNRAS*, 476, 961
- Galametz A. et al., 2013, *A&A*, 559, A2
- García-Vergara C. et al., 2022, *ApJ*, 927, 65
- Geach J. E. et al., 2017, *MNRAS*, 465, 1789
- Glazebrook K. et al., 2017, *Nature*, 544, 71
- Gobat R. et al., 2018, *Nat. Astron.*, 2, 239
- Gobat R., Magdis G., D'Eugenio C., Valentino F., 2020, *A&A*, 644, L7
- Gómez-Guijarro C. et al., 2019, *ApJ*, 872, 117



- Goto T., Utsumi Y., Kikuta S., Miyazaki S., Shiki K., Hashimoto T., 2017, *MNRAS*, 470, L117
- Graziani L., Schneider R., Ginolfi M., Hunt L. K., Maio U., Glatzle M., Ciardi B., 2020, *MNRAS*, 494, 1071
- Guaita L. et al., 2022, *A&A*, 660, A137
- Hagimoto M. et al., 2023, *MNRAS*, 521, 5508
- Hainline L. J., Blain A. W., Smail I., Alexander D. M., Armus L., Chapman S. C., Ivison R. J., 2011, *ApJ*, 740, 96
- Harrington K. C. et al., 2021, *ApJ*, 908, 95
- Harrison I., Hotchkiss S., 2013, *J. Cosmol. Astropart. Phys.*, 2013, 022
- Hatch N. A., Kurk J. D., Pentericci L., Venemans B. P., Kuiper E., Miley G. K., Röttgering H. J. A., 2011, *MNRAS*, 415, 2993
- Hickox R. C. et al., 2012, *MNRAS*, 421, 284
- Hill R. et al., 2020, *MNRAS*, 495, 3124
- Hlavacek-Larrondo J. et al., 2020, *ApJ*, 898, L50
- Hodge J. A., da Cunha E., 2020, *R. Soc. Open Sci.*, 7, 200556
- Hodge J. A., Carilli C. L., Walter F., Daddi E., Riechers D., 2013, *ApJ*, 776, 22
- Holland W. S. et al., 2013, *MNRAS*, 430, 2513
- Holland W. S. et al., 2017, *MNRAS*, 470, 3606
- Hopkins P. F., Hernquist L., Cox T. J., Kereš D., 2008, *ApJS*, 175, 356
- Ikarashi S. et al., 2015, *ApJ*, 810, 133
- Ismail D. et al., 2023, *A&A*, 678, A27
- Ito K. et al., 2022, *ApJ*, 929, 53
- Ivison R. J., Dunlop J. S., Smail I., Dey A., Liu M. C., Graham J. R., 2000, *ApJ*, 542, 27
- Ivison R. J. et al., 2016, *ApJ*, 832, 78
- Karim A. et al., 2013, *MNRAS*, 432, 2
- Kennicutt Robert C. J., 1998, *ARA&A*, 36, 189
- Kikuta S., Imanishi M., Matsuoka Y., Matsuda Y., Shimasaku K., Nakata F., 2017, *ApJ*, 841, 128
- Kikuta S. et al., 2019, *PASJ*, 71, L2
- Kim S. et al., 2009, *ApJ*, 695, 809
- Koyama Y., Kodama T., Tadaki K.-i., Hayashi M., Tanaka M., Smail I., Tanaka I., Kurk J., 2013, *MNRAS*, 428, 1551
- Koyama Y. et al., 2021, *MNRAS*, 503, L1
- Kubo M. et al., 2019, *ApJ*, 887, 214
- Kuiper E. et al., 2011, *MNRAS*, 415, 2245
- Kurk J. D. et al., 2000, *A&A*, 358, L1
- Lacaille K. M. et al., 2019, *MNRAS*, 488, 1790
- Lee M. M., Tanaka I., Iono D., Kawabe R., Kodama T., Kohno K., Saito T., Tamura Y., 2021, *ApJ*, 909, 181
- Lehmer B. D. et al., 2009, *MNRAS*, 400, 299
- Lewis A. J. R. et al., 2018, *ApJ*, 862, 96
- Litke K. C. et al., 2022, *ApJ*, 928, 179
- Long A. S. et al., 2020, *ApJ*, 898, 133
- Looser T. J. et al., 2023, preprint ([arXiv:2302.14155](https://arxiv.org/abs/2302.14155))
- Madau P., Dickinson M., 2014, *ARA&A*, 52, 415
- Magnelli B. et al., 2015, *A&A*, 573, A45
- Mairs S. et al., 2021, *AJ*, 162, 191
- Man A., Belli S., 2018, *Nat. Astron.*, 2, 695
- Mantz A. B. et al., 2014, *ApJ*, 794, 157
- Mazzucchelli C., Bañados E., Decarli R., Farina E. P., Venemans B. P., Walter F., Overzier R., 2017, *ApJ*, 834, 83
- McBride J., Fakhouri O., Ma C.-P., 2009, *MNRAS*, 398, 1858
- Meinke J., Böckmann K., Cohen S., Mauskopf P., Scannapieco E., Sarmento R., Lunde E., Cottle J., 2021, *ApJ*, 913, 88
- Merlin E. et al., 2019, *MNRAS*, 490, 3309
- Millard J. S. et al., 2020, *MNRAS*, 494, 293
- Miller T. B. et al., 2018, *Nature*, 556, 469
- Morselli L. et al., 2014, *A&A*, 568, A1
- Mountrichas G., Masoura V. A., Xilouris E. M., Georgantopoulos I., Buat V., Paspaliaris E. D., 2022, *A&A*, 661, A108
- Muldrew S. I., Hatch N. A., Cooke E. A., 2015, *MNRAS*, 452, 2528
- Negrello M. et al., 2010, *Science*, 330, 800
- Negrello M. et al., 2017, *MNRAS*, 465, 3558
- Neri R. et al., 2020, *A&A*, 635, A7
- Newman A. B., Ellis R. S., Andreon S., Treu T., Raichoor A., Trinchieri G., 2014, *ApJ*, 788, 51
- Noble A. G. et al., 2017, *ApJ*, 842, L21
- Ota K. et al., 2018, *ApJ*, 856, 109
- Oteo I. et al., 2018, *ApJ*, 856, 72
- Overzier R. A., 2016, *A&AR*, 24, 14
- Pantoni L., Lapi A., Massardi M., Goswami S., Danese L., 2019, *ApJ*, 880, 129
- Pâris I. et al., 2018, *A&A*, 613, A51
- Pearson E. A. et al., 2013, *MNRAS*, 435, 2753
- Peng Y., Maiolino R., Cochrane R., 2015, *Nature*, 521, 192
- Pérez-Martínez J. M. et al., 2023, *MNRAS*, 518, 1707
- Péroux C., Howk J. C., 2020, *ARA&A*, 58, 363
- Planck Collaboration VI, 2020, *A&A*, 641, A6
- Popping G., Péroux C., 2022, *MNRAS*, 513, 1531
- Remus R.-S., Dolag K., Dannerbauer H., 2022, *ApJ*, 950, 191
- Richards G. T. et al., 2009, *ApJS*, 180, 67
- Richards G. T. et al., 2015, *ApJS*, 219, 39
- Riechers D. A., Cooray A., Pérez-Fournon I., Neri R., 2021, *ApJ*, 913, 141
- Rowan-Robinson M. et al., 2016, *MNRAS*, 461, 1100
- Schreiber C. et al., 2018, *A&A*, 618, A85
- Scott S. E. et al., 2002, *MNRAS*, 331, 817
- Scoville N. et al., 2016, *ApJ*, 820, 83
- Scudder J. M., Oliver S., Hurley P. D., Griffin M., Sargent M. T., Scott D., Wang L., Wardlow J. L., 2016, *MNRAS*, 460, 1119
- Seymour N. et al., 2012, *ApJ*, 755, 146
- Shimakawa R., Kodama T., Tadaki K.-i., Hayashi M., Koyama Y., Tanaka I., 2015, *MNRAS*, 448, 666
- Shimakawa R. et al., 2018, *MNRAS*, 473, 1977
- Shimwell T. W. et al., 2022, *A&A*, 659, A1
- Shirley R. et al., 2021, *MNRAS*, 507, 129
- Simpson J. M. et al., 2017, *ApJ*, 839, 58
- Simpson J. M. et al., 2019, *ApJ*, 880, 43
- Smail I., 2024, *MNRAS*, 529, 2290
- Smail I., Swinbank A. M., Ivison R. J., Ibar E., 2011, *MNRAS*, 414, L95
- Smith M. W. L. et al., 2017, *ApJS*, 233, 26
- Smith M. W. L. et al., 2019a, *MNRAS*, 486, 4166
- Smith C. M. A., Gear W. K., Smith M. W. L., Papageorgiou A., Eales S. A., 2019b, *MNRAS*, 486, 4304
- Solomon P. M., Vanden Bout P. A., 2005, *ARA&A*, 43, 677
- Spilker J. S., Bezanson R., Marrone D. P., Weiner B. J., Whitaker K. E., Williams C. C., 2016, *ApJ*, 832, 19
- Spilker J. S. et al., 2018, *Science*, 361, 1016
- Spilker J. S. et al., 2020a, *ApJ*, 905, 85
- Spilker J. S. et al., 2020b, *ApJ*, 905, 86
- Spitler L. R. et al., 2012, *ApJ*, 748, L21
- Stach S. M., Swinbank A. M., Smail I., Hilton M., Simpson J. M., Cooke E. A., 2017, *ApJ*, 849, 154
- Stach S. M. et al., 2021, *MNRAS*, 504, 172
- Stanford S. A. et al., 2012, *ApJ*, 753, 164
- Stanley F. et al., 2023, *ApJ*, 945, 24
- Steidel C. C., Adelberger K. L., Dickinson M., Giavalisco M., Pettini M., Kellogg M., 1998, *ApJ*, 492, 428
- Stevens J. A. et al., 2003, *Nature*, 425, 264
- Stevens J. A., Page M. J., Ivison R. J., Carrera F. J., Mittaz J. P. D., Smail I., McHardy I. M., 2005, *MNRAS*, 360, 610
- Stevens J. A., Jarvis M. J., Coppin K. E. K., Page M. J., Greve T. R., Carrera F. J., Ivison R. J., 2010, *MNRAS*, 405, 2623
- Straatman C. M. S. et al., 2014, *ApJ*, 783, L14
- Sweijen F. et al., 2022, *Nat. Astron.*, 6, 350
- Swinbank A. M. et al., 2014, *MNRAS*, 438, 1267
- Tadaki K.-i. et al., 2019, *PASJ*, 71, 40
- Tamura Y. et al., 2009, *Nature*, 459, 61
- Toft S. et al., 2014, *ApJ*, 782, 68
- Toshikawa J. et al., 2012, *ApJ*, 750, 137
- Tran K.-V. H. et al., 2015, *ApJ*, 811, 28
- Treu T., 2010, *ARA&A*, 48, 87

- Trudeau A. et al., 2019, *MNRAS*, 487, 1210
- Umehata H. et al., 2015, *ApJ*, 815, L8
- Urquhart S. A. et al., 2022, *MNRAS*, 511, 3017
- Utsumi Y., Goto T., Kashikawa N., Miyazaki S., Komiyama Y., Furusawa H., Overzier R., 2010, *ApJ*, 721, 1680
- Valentino F. et al., 2015, *ApJ*, 801, 132
- Valiante E. et al., 2016, *MNRAS*, 462, 3146
- van der Burg R. F. J., Muzzin A., Hoekstra H., Wilson G., Lidman C., Yee H. K. C., 2014, *A&A*, 561, A79
- van Haarlem M. P. et al., 2013, *A&A*, 556, A2
- Vayner A., Zakamska N., Wright S. A., Armus L., Murray N., Walth G., 2021, *ApJ*, 923, 59
- Venemans B. P. et al., 2007, *A&A*, 461, 823
- Vieira J. D. et al., 2013, *Nature*, 495, 344
- Vijayan A. P., Clay S. J., Thomas P. A., Yates R. M., Wilkins S. M., Henriques B. M., 2019, *MNRAS*, 489, 4072
- Walter F. et al., 2012, *Nature*, 486, 233
- Walter F. et al., 2020, *ApJ*, 902, 111
- Wang W., Wylezalek D., De Breuck C., Vernet J., Humphrey A., Villar Martín M., Lehnert M. D., Kolwa S., 2021, *A&A*, 654, A88
- Webb T. M. A. et al., 2015, *ApJ*, 814, 96
- Webb T. M. A. et al., 2017, *ApJ*, 844, L17
- Wei A. et al., 2009, *ApJ*, 707, 1201
- Wilson G. W. et al., 2020, Proc. SPIE Conf. Ser. Vol. 11453, Society of Photo-Optical Instrumentation Engineers, SPIE, Bellingham, p. 1145302
- Wright E. L. et al., 2010, *AJ*, 140, 1868
- Yuan T. et al., 2014, *ApJ*, 795, L20
- Zavala J. A. et al., 2015, *MNRAS*, 452, 1140
- Zavala J. A. et al., 2019, *ApJ*, 887, 183
- Zeballos M. et al., 2018, *MNRAS*, 479, 4577
- Zeimann G. R. et al., 2012, *ApJ*, 756, 115
- Zhang Y. et al., 2022, *MNRAS*, 512, 4893

## APPENDIX: SPECTRAL FITTING USING HERSCHEL AND SCUBA-2 FLUXES

Fig. A1 shows the fits of the six sources detected at  $>5\sigma$  (with *solid black borders* in Fig. 9). While multiple sources are not detected in the *Herschel* catalogues, these observations provide strict upper limits (particularly at the wavelength of 250  $\mu\text{m}$ ) that restrict the potential photometric redshifts of these sources. The *red line* shows the fitted spectrum according to the two-temperature modified black-body of Pearson et al. (2013), while the *blue* and *grey lines* indicate the best-fitting spectrum according to the method presented in Ivison et al. (2016). Both methods appear to fit the data well.

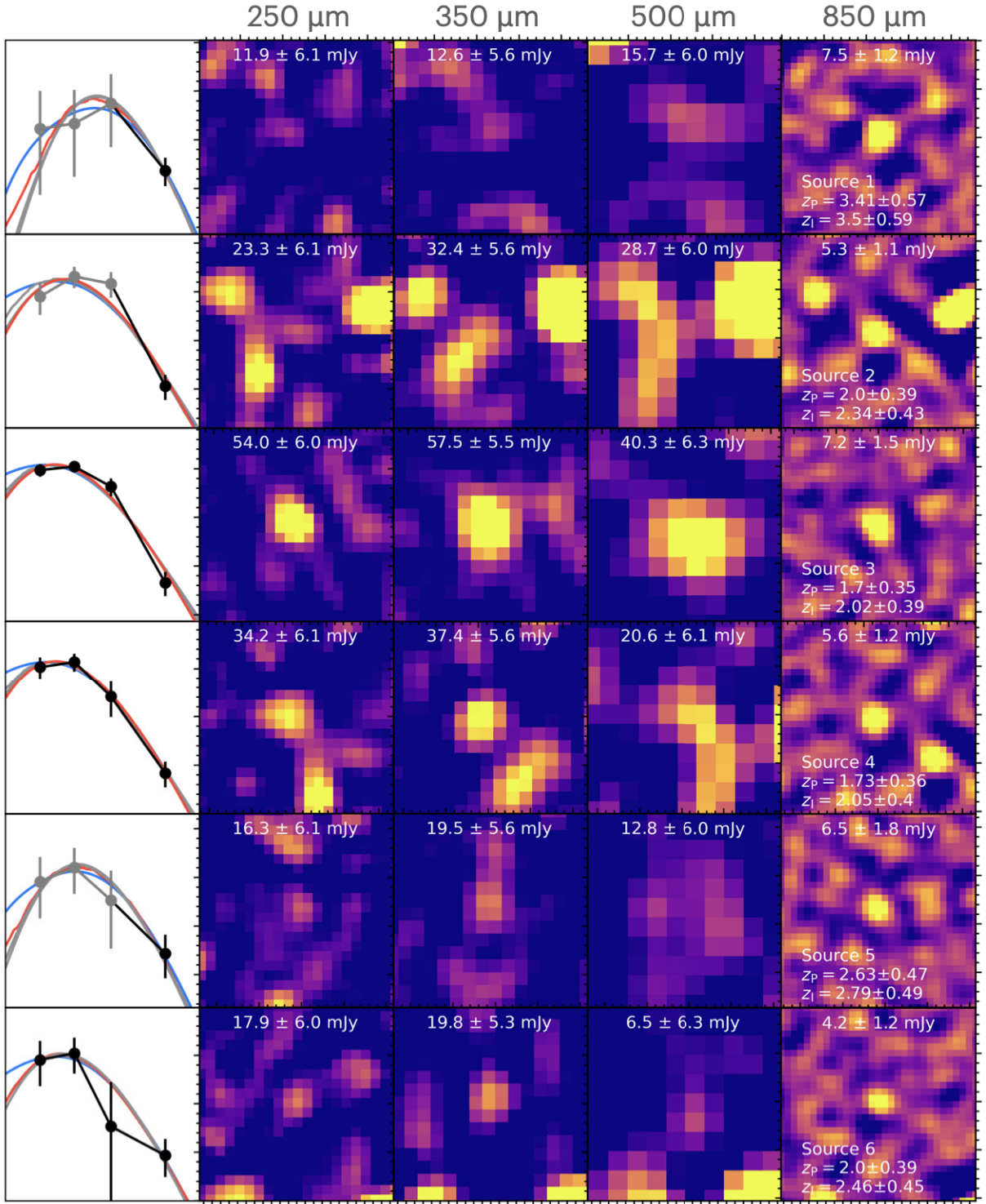


**Figure A1.** The left columns show the fitted spectra (*black markers* for detected sources and *grey markers* for sources without a listing in the HELP catalogue), with *red line* indicating the two-temperature modified black-body from Pearson et al. (2013) (indicated by  $z_p$ ), *blue line* indicating the best-fitting spectrum from the Ivison et al. (2016) method (indicated by  $z_l$ ), and the grey lines showing the fitted templates with higher SNRs. From left to right, the images show the 250, 350, 500, and 850  $\mu\text{m}$  maps at 1 by 1 arcmin. The photometric redshift estimates of all six sources agree with the spectroscopic redshift of HerBS-70E&W at  $z_{\text{spec}} = 2.3$ .

- <sup>1</sup>Department of Earth and Space Sciences, Chalmers University of Technology, Onsala Observatory, SE-439 94 Onsala, Sweden
- <sup>2</sup>Department of Physics, Graduate School of Science, Nagoya University, Nagoya, Aichi 464-8602, Japan
- <sup>3</sup>National Astronomical Observatory of Japan, 2-21-1, Osawa, Mitaka, Tokyo 181-8588, Japan
- <sup>4</sup>Institut de Radioastronomie Millimétrique (IRAM), 300 Rue de la Piscine, F-38400 Saint-Martin-d'Hères, France
- <sup>5</sup>Instituto Astrofísica de Canarias (IAC), E-38205 La Laguna, Tenerife, Spain
- <sup>6</sup>Dpto. Astrofísica, Universidad de la, E-38206 La Laguna, Tenerife, Spain
- <sup>7</sup>Institut d'Astrophysique de Paris, Sorbonne Université, UPMC Université Paris 6 and CNRS, UMR 7095, 98 bis boulevard Arago, F-75014 Paris, France
- <sup>8</sup>Instituto Nacional de Astrofísica, Óptica y Electrónica, Tonantzintla, 72000 Puebla, México
- <sup>9</sup>I. Physikalisches Institut, Universität zu Köln, Zùlpicher Strasse 77, D-50937 Köln, Germany
- <sup>10</sup>Leiden Observatory, Leiden University, PO Box 9513, NL-2300 RA Leiden, the Netherlands
- <sup>11</sup>Department of Physics and Astronomy, Rutgers, the State University of New Jersey, 136 Frelinghuysen Road, Piscataway, NJ 08854-8019, USA
- <sup>12</sup>Department of Physics and Astronomy, University of the Western Cape, Robert Sobukwe Road, Bellville 7535, South Africa
- <sup>13</sup>Institut d'Astrophysique Spatiale (IAS), CNRS et Université Paris Sud, 13013, Orsay, France
- <sup>14</sup>UK ALMA Regional Centre Node, Jodrell Bank Centre for Astrophysics, Department of Physics and Astronomy, University of Manchester, Oxford Road, Manchester M13 9PL, UK
- <sup>15</sup>Dipartimento di Fisica e Astronomia 'G. Galilei', Università di Padova, Vicolo dell'Osservatorio 3, I-35122, Padova, Italy
- <sup>16</sup>Aix-Marseille Université, CNRS and CNES, Laboratoire d'Astrophysique de Marseille, 38, rue Frédéric Joliot-Curie, F-13388 Marseille, France
- <sup>17</sup>Department of Physics & Astronomy, University of California, Irvine, 4129 Reines Hall, Irvine, CA 92697, USA
- <sup>18</sup>School of Physics and Astronomy, Cardiff University, The Parade, Cardiff CF24 3AA, UK
- <sup>19</sup>School of Physics & Astronomy, University of Nottingham, University Park, Nottingham NG7 2RD, UK
- <sup>20</sup>Institute of Astronomy, University of Cambridge, Madingley Road, Cambridge CB30HA, UK
- <sup>21</sup>Department of Astronomy, University of Maryland, College Park, MD 20742, USA
- <sup>22</sup>European Southern Observatory, Karl Schwarzschild Strasse 2, D-85748 Garching, Germany
- <sup>23</sup>Jodrell Bank Centre for Astrophysics, School of Natural Sciences, The University of Manchester, Manchester M13 9PL, UK
- <sup>24</sup>Centre de Recherche Astrophysique de Lyon, ENS de Lyon, Université Lyon 1, CNRS, UMR5574, F-69230 Saint-Genis-Laval, France
- <sup>25</sup>Department of Astronomy, University of Cape Town, Private Bag X3, Rondebosch 7701, Cape Town, South Africa
- <sup>26</sup>INAF, Istituto di Radioastronomia-Italian ARC, Via Piero Gobetti 101, I-40129 Bologna, Italy
- <sup>27</sup>European Southern Observatory, Alonso de Córdova 3107, Vitacura, Casilla 19001, Santiago de Chile, Chile
- <sup>28</sup>Joint ALMA Observatory, Alonso de Córdova 3107, Vitacura 763-0355, Santiago de Chile, Chile
- <sup>29</sup>Ikerbasque Foundation, University of the Basque Country, DIPIC Donostia, 48009, Spain
- <sup>30</sup>National Centre for Nuclear Research, ul. Pasteura 7, PL-02-093 Warszawa, Poland
- <sup>31</sup>INAF – Osservatorio astronomico d'Abruzzo, Via Maggini SNC, I-64100, Teramo, Italy
- <sup>32</sup>The Observatories of the Carnegie Institution for Science, 813 Santa Barbara St., Pasadena, CA 91101, USA
- <sup>33</sup>Department of Physics and Astronomy, University of California, Riverside, 900 University Ave, Riverside, CA 92521, USA
- <sup>34</sup>School of Physical Sciences, The Open University, Milton Keynes, MK7 6AA, UK
- <sup>35</sup>National Radio Astronomy Observatory, 520 Edgemont Road, Charlottesville, VA 22903, USA
- <sup>36</sup>Max-Planck-Institut für Radioastronomie, Auf dem Hügel 69, D-53121 Bonn, Germany

This paper has been typeset from a  $\text{\LaTeX}$  file prepared by the author.